

Cloud Microphysical Processes and Atmospheric Water Budget during the 20 July 2021 Extreme Precipitation Event in Zhengzhou, China

Weixi SHU^{1,2}, Danhong FU^{1,2*}, Hui XIAO^{1,2}, Huiling YANG¹, Yue SUN¹, Xueliang GUO^{1,2}, Yang ZHAO³, Jianfang DING⁴, and Shujing SHEN⁵

¹ Key Laboratory of Cloud–Precipitation Physics and Severe Storms (LACS), Institute of Atmospheric Physics, Chinese Academy of Sciences, Beijing 100029

² School of Earth and Planetary Sciences, University of Chinese Academy of Sciences, Beijing 100049

³ School of Earth and Space Sciences, University of Science and Technology of China, Hefei 230026

⁴ Weather Modification Center of Henan Province, Zhengzhou 450003

⁵ CMA Cloud–Precipitation Physics and Weather Modification Key Laboratory, Weather Modification Centre, China Meteorological Administration (CMA), Beijing 100081

(Received 11 November 2022; in final form 2 June 2023)

ABSTRACT

This study investigated the cloud microphysical processes and atmospheric water budget during the extreme precipitation event on 20 July 2021 in Zhengzhou of Henan Province, China, based on observations, reanalysis data, and the results from the high-resolution large-eddy simulation nested in the Weather Research and Forecasting (WRF) model with assimilation of satellite and radar observations. The results show that the abundant and persistent southeasterly supply of water vapor, induced by Typhoons In-Fa and Cempaka, under a particular synoptic pattern featured with abnormal northwestward displacement of the western Pacific subtropical high, was conducive to warm rain processes through a high vapor condensation rate of cloud water and an efficient collision–coalescence process of cloud water to rainwater. Such conditions were favorable for the formation and maintenance of the quasi-stationary warm-sector heavy rainfall. Precipitation formation through the collision–coalescence process of cloud water to rainwater accounted for approximately 70% of the total, while the melting of snow and graupel accounted for only approximately 30%, indicating that warm cloud processes played a dominant role in this extreme rainfall event. However, enhancement of cold cloud processes promoted by latent heat release also exerted positive effect on rainfall during the period of most intense hourly rainfall. It was also found that rainwater advection from outside of Zhengzhou City played an important role in maintaining the extreme precipitation event.

Key words: extreme precipitation event, microphysical processes, atmospheric water budget, large-eddy simulation

Citation: Shu, W. X., D. H. Fu, H. Xiao, et al., 2023: Cloud microphysical processes and atmospheric water budget during the 20 July 2021 extreme precipitation event in Zhengzhou, China. *J. Meteor. Res.*, **37**(5), 722–742, doi: 10.1007/s13351-023-2166-y.

1. Introduction

The complex topography and climate of China result in frequent high-intensity precipitation events and flash floods (Wu et al., 2018). Urban floods are particularly devastating, causing substantial economic losses and human fatalities (Zhang et al., 2017; Tellman et al., 2021). Henan Province in central China is one area prone to serious rainstorm disasters (Ding, 2015; Wu et al., 2021).

Heavy rainfall in this region exhibits the characteristics of high intensity, long duration, and considerable abruptness, despite this area having lower annual precipitation amount in comparison with some other areas in southern China (Zhang, 2014).

An extreme rainfall event occurred in Zhengzhou of Henan Province, China on 20 July 2021. The 24-h cumulative rainfall from 0000 UTC 20 to 0000 UTC 21 July 2021 in Zhengzhou reached 624.1 mm, exceeding its

Supported by the National Key Research and Development Program of China (2016YFE0201900-02 and 2019YFC1510304) and National Natural Science Foundation of China (41575037).

*Corresponding author: fudanhong@mail.iap.ac.cn

© The Chinese Meteorological Society and Springer-Verlag Berlin Heidelberg 2023

total annual precipitation in 2019 (Sun et al., 2021). The maximum rainfall intensity reached a record-breaking 201.9 mm h^{-1} during 0800–0900 UTC 20 July in Zhengzhou. The resultant high casualties (including a death toll of approximately 380) and vast property damages (direct economic loss of 409 billion Yuan), and the underprediction of the precipitation by all operational numerical weather prediction models, have aroused widespread concern and attention.

Recent studies suggested that the factors that could have played a role in this extreme precipitation event include instability of the atmosphere, abnormally strong water vapor transport from the East China coast, topographic effects, and stagnation of the convective system over Zhengzhou (Ran et al., 2021; Su et al., 2021; Chyi et al., 2022). Additionally, sharp increase in hydrometeors from the southern boundary of Zhengzhou City could have also promoted the heavy precipitation (Sun et al., 2021). Analysis of high-resolution numerical simulations indicated that the contribution from the unique dynamic structure of the well-organized meso- γ -scale convective system to the record-breaking rainfall was important, and the extreme precipitation may also be caused by interactions between cloud microphysical processes and the horizontal transport of rainwater from outside of Zhengzhou (Yin et al., 2022).

Precipitation is produced directly by the cloud microphysical processes, which interact with meso-, synoptic-, and large-scale dynamic and thermodynamic processes. Cloud microphysics and the convergence of water vapor are important factors that determine the precipitation rate (Gao et al., 2005; Shen et al., 2011; Van Weverberg et al., 2011; Yang et al., 2015). Previous studies indicated that water vapor transport related and hydrometeor-related cloud microphysical processes significantly impact the surface precipitation (Rauber et al., 2000; Huang and Cui, 2015). Huang et al. (2016) studied a topographic rainfall event and found that moisture advection played a dominant role in the event and the moisture flux convergence was a major factor, whereas cloud microphysical processes were less contributory. Lu et al. (2021) studied an isolated storm-triggered heavy precipitation event and suggested that the contribution from moisture advection to the precipitation was only slightly higher than that from cloud microphysics-related process. Huang et al. (2019a) analyzed a heavy rainfall event and found that the magnitude of the precipitation budget in the convective region was one order larger than that in the stratiform region.

Clouds are intimately related to precipitation. Cold and warm clouds play different roles in precipitation gen-

eration and development. Some studies suggested that cold cloud processes have a dominant role in generating heavy precipitation and that rainfall is mainly produced by the melting of large ice-phase particles (Rauber et al., 2000; Franklin et al., 2005; Zhu and Zhang, 2006; Huang and Cui, 2015). Unlike a precipitation system dominated by cold cloud processes, a system dominated by warm cloud processes has a lower cloud top height and weaker interactions between liquid- and ice-phase particles, and the rainfall could be heavy given a sufficient supply of water vapor (Chen et al., 2005; Song et al., 2017). The simulation of several heavy precipitation events was found improved by better simulation of warm cloud processes (Song and Sohn, 2018). Based on polarimetric radar observations, Chang et al. (2015) postulated that heavy rainfall can be efficiently produced by enhanced coalescence and accretion growth of raindrops in conditions with high cloud water content at low levels. Wang et al. (2016) assessed polarimetric radar measurements, estimated the profiles of vertical liquid components, and suggested that the conversion of cloud water into rainwater plays a dominant role in producing heavy rainfall.

To understand the formation mechanisms of the extreme precipitation event on 20 July 2021 in Zhengzhou of central China, this study will investigate the cloud microphysical processes and atmospheric water budget based on various observations, the fifth-generation ECMWF reanalysis (ERA5) data, and the results from the high-resolution large-eddy simulation (LES) nested in the Weather Research and Forecasting (WRF) model, which has switched on the assimilation of various available observations.

The remainder of this paper is organized as follows. Section 2 describes the data and methods used in the study. Section 3 provides an overview of the extreme precipitation case. Section 4 describes the characteristics of the cloud microphysical processes and atmospheric water budget of the studied extreme precipitation event. Finally, Section 5 presents the conclusions along with a brief discussion.

2. Data and methods

2.1 Data

This study utilized conventional meteorological data from automatic weather stations (<https://data.cma.cn/data/cdcdetail/dataCode/A.0012.0001.html>) and radar observations acquired at Zhengzhou station, which were provided by the China National Meteorological Data Centre (<https://data.cma.cn/data/cdcindex/cid/227aa07a9079550a.html>). The dataset has been used extensively in

other meteorological studies (Fu et al., 2018; Wang et al., 2021). The observations were analyzed to examine the characteristics of the cloud structure and to validate the numerical simulations. The ERA5 product at 3-h intervals with spatial resolution of $0.25^\circ \times 0.25^\circ$ from 2100 UTC 19 to 0000 UTC 21 July 2021 (<https://cds.climate.copernicus.eu/cdsapp#!/search?type=dataset>) was used to initiate the WRF model.

2.2 Model and its setup

The WRF model v4.1.2 (Skamarock et al., 2008) was employed. Four nested model domains, i.e., d01, d02, d03, and d04 (Fig. 1), were configured with horizontal grids of 631×393 , 625×547 , 595×586 , and 400×244 points and resolutions of 9 km, 3 km, 1 km, and 333.333 m, respectively, with 57 vertical levels up to 20 hPa; and the model time step is 27, 9, 3, and 1 s, respectively. The simulation period extended from 2100 UTC 19 to 0000 UTC 21 July 2021, and the data from d04 were output every 10 min.

The LES approach is effective in capturing local small-scale atmospheric motions because it explicitly resolves large turbulent eddies and cloud microphysics, and can better simulate both the wind field and the water vapor convergence in the boundary layer (Zhu et al., 2017; Liu et al., 2018; Li et al., 2021), beneficial for forecasting initiation of convection (Kang and Bryan, 2011). For these reasons, in comparison with mesoscale numerical simulations, the LES can provide more accurate representation of turbulent high-energy motion, especially in heavy precipitation events (Heath et al., 2017; Huang et al., 2019b; Stevens et al., 2020). Therefore, this study used the LES within the WRF package (WRF-LES) in d04. To accommodate the requirement for high-

resolution terrain in the LES, the topographic data used in d04 were sourced from the 3-arc-second-resolution (90-m) Shuttle Radar Topography Mission dataset (De Meij and Vinuesa, 2014; <https://srtm.csi.cgiar.org/>) (Fig. 1b).

In this study, two-way interaction was used in the WRF model, and the LES ran on the smallest nested domain (d04). The Yonsei University planetary boundary layer (PBL) scheme (Hong et al., 2006) was used for d01, d02, and d03, but was not activated for d04, where a gradient method with full metric terms was used to accurately compute horizontal gradients in sloped coordinates, and a 1.5-order turbulent kinetic energy closure condition was used. Additionally, the Kain–Fritsch cumulus parametrization (Kain, 2004) was used for d01. Other physical parameterization schemes were consistent in all four domains, including the Rapid Radiative Transfer Model for general circulation models (RRTMG) longwave and shortwave radiation schemes (Iacono et al., 2008), the Unified Noah land surface scheme (Chen and Dudhia, 2001), and the Mesoscale Model version 5 (MM5) Monin–Obukhov similarity scheme (Zhang and Anthes, 1982). The Morrison double-moment cloud microphysics scheme (Morrison et al., 2009) was applied in d02, d03, and d04, which describes the complex microphysical processes of five hydrometeor particles: cloud water, rainwater, cloud ice, snow, and graupel.

The NCEP operational global surface and upper-air observation subsets at 3-h intervals from 2100 UTC 19 to 0000 UTC 21 July 2021 (<https://rda.ucar.edu/datasets/ds351.0>; <https://rda.ucar.edu/datasets/ds461.0>) were used to conduct objective analysis (Lazarus et al., 2002) to reduce the error of the ERA5 data. Following objective analysis, ERA5 data for 2100 UTC 19 July 2021 were

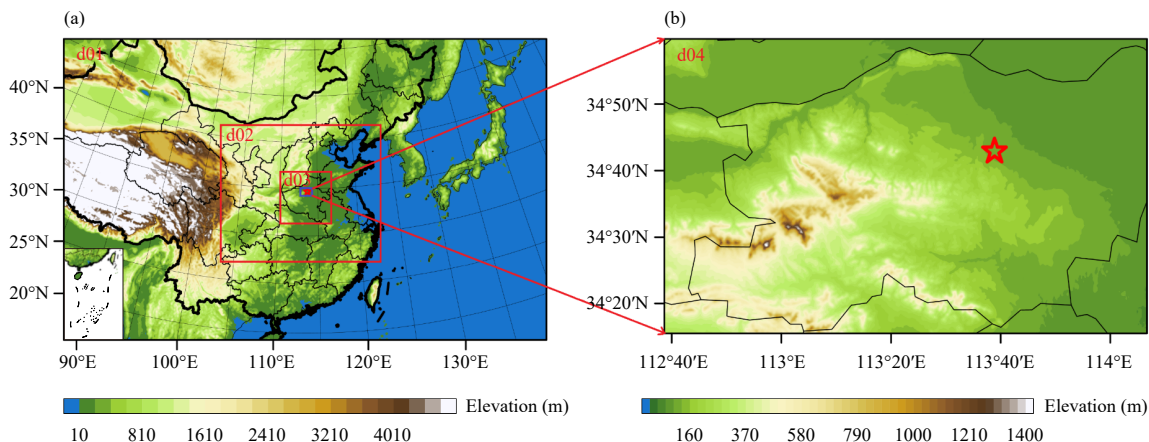


Fig. 1. Simulation domains and terrain elevation (shading; m). The Zhengzhou station is marked with a bold red star. The black lines in (b) represent the borders of cities within Henan Province of China.

used as the initial conditions, and the boundary conditions were available every 3 hours from the ERA5 data (after objective analysis).

To improve the simulation, various observational data were assimilated. The brightness temperature data (<https://rda.ucar.edu/datasets/ds735.0>) from the Advanced Television Infrared Observation Satellite (TIROS) Operational Vertical Sounder were assimilated every 6 hours (i.e., at 0000, 0600, 1200, and 1800 UTC 20 July 2021) to improve the wind, humidity, pressure, and temperature fields (Saunders, 1993). The three-dimensional (3D) radar reflectivity mosaic data from the operational system of the Institute of Beijing Urban Meteorology of China Meteorological Administration were also assimilated every 6 hours (i.e., at 0000, 0600, 1200, and 1800 UTC 20 July 2021) to improve the representation of cloud hydrometeors such as rainwater, snow, and graupel through retrievals from radar reflectivity (He et al., 2019). Meanwhile, to maintain consistency between the meteorological fields in the simulation process and the large-scale meteorological fields, grid analysis nudging technology (Eiserloh and Chiao, 2015) was introduced using the reanalysis data every 3 hours (adjusted by objective analysis) from 2100 UTC 19 to 0000 UTC 21 July 2021.

2.3 Atmospheric water budget and cloud microphysics

To understand the formation mechanisms of the studied extreme precipitation event, quantitative contributions of water-vapor-related and hydrometeor-related processes to the precipitation rate were analyzed based on the simulation results.

Based on the two-dimensional (2D) rainfall diagnostic equation of Gao et al. (2005), Huang et al. (2016) proposed a 3D precipitation equation according to the water vapor and hydrometeor budgets of the WRF model (Skamarock et al., 2008). The equation directly links the precipitation rate to the water vapor and hydrometeor budgets, providing detailed insight into the physical mechanisms. The equation can be expressed simply as follows,

$$P_S = Q_{WV} + Q_{CM}. \quad (1)$$

According to Eq. (1), the surface precipitation rate (P_S) is determined by the water-vapor-related rate (Q_{WV}) and the hydrometeor-related rate (Q_{CM}). Q_{WV} can be expressed as,

$$Q_{WV} = Q_{WVL} + Q_{WVA} + Q_{WVE} + Q_{WVD}, \quad (2)$$

where Q_{WVL} , Q_{WVA} , Q_{WVE} , and Q_{WVD} represent the local rates of change in water vapor, 3D moisture advection,

surface evaporation, and 3D moisture diffusion, respectively. Q_{CM} can be expressed as,

$$Q_{CM} = Q_{CLL} + Q_{CLA} + Q_{CLD} + Q_{CIL} + Q_{CIA} + Q_{CID}, \quad (3)$$

where Q_{CLL} , Q_{CLA} , and Q_{CLD} denote the local rates of change in liquid-phase particles, 3D advection of liquid-phase particles, and 3D diffusion of liquid-phase particles, respectively. Q_{CLL} includes the local rates of change in cloud water (Q_{CCLOL}) and rainwater (Q_{CRAIL}). Q_{CLA} includes the 3D advection of cloud water (Q_{CCLOA}) and rainwater (Q_{CRAIA}). Q_{CIL} , Q_{CIA} , and Q_{CID} represent the local rates of change in ice-phase particles, 3D advection of ice-phase particles, and 3D diffusion of ice-phase particles, respectively. Q_{CIL} includes the local rates of change in cloud ice (Q_{CICEL}), snow (Q_{CSNOL}), and graupel (Q_{CGRAL}). Q_{CIA} includes the 3D advection of cloud ice (Q_{CICEA}), snow (Q_{CSNOA}), and graupel (Q_{CGRAA}). In Eqs. (2) and (3), the diffusion terms Q_{WVD} , Q_{CLD} , and Q_{CID} can be neglected because the magnitude of each is comparatively very small (Liu and Cui, 2018; Xu et al., 2018). Additional details regarding the above physical processes can be found in Huang et al. (2016) and Wang X. H. et al. (2019). The WRF-based 3D precipitation equation has been used to diagnose and investigate rainfall processes and formation mechanisms (Huang et al., 2019a; Wu et al., 2020; Lu et al., 2021).

To analyze the microphysical processes in the studied extreme precipitation event, the relative contributions of the microphysical processes related to rainwater, snow, and graupel are investigated and calculated by using the following Eq. (4):

$$RC_x = \frac{Q_x}{Q_{sum}}, \quad (4)$$

where RC_x represents the relative contribution of process x , Q_x is the mixing ratio for hydrometeor particles produced by process x , and Q_{sum} represents the sum of the mixing ratios for all processes involving a certain hydrometeor.

To analyze the changes and impacts of latent heat in the precipitation process, the latent heat rates of condensation, freezing, deposition, evaporation, and melting are calculated by using Eqs. (5)–(9):

$$Q_{CON} = L_v \times P_{CON}/C_{pm}, \quad (5)$$

$$Q_{FRZ} = L_f \times P_{FRZ}/C_{pm}, \quad (6)$$

$$Q_{DEP} = L_s \times P_{DEP}/C_{pm}, \quad (7)$$

$$Q_{EVP} = L_v \times P_{EVP}/C_{pm}, \quad (8)$$

$$Q_{MLT} = L_f \times P_{MLT}/C_{pm}, \quad (9)$$

where Q_{CON} , Q_{FRZ} , Q_{DEP} , Q_{EVP} , and Q_{MLT} represent the latent heat rates (K min^{-1}) related to the processes of condensation, freezing, deposition, evaporation, and melting, respectively; L_v , L_f , and L_s are the latent heat of condensation, fusion, and sublimation, respectively; C_{pm} is the specific heat of moist air at constant pressure; and P_{CON} , P_{FRZ} , P_{DEP} , P_{EVP} , and P_{MLT} are the mass production rates ($\text{kg kg}^{-1} \text{min}^{-1}$) of the microphysical processes related to condensation, freezing and riming, deposition, evaporation, and melting, respectively. Full descriptions of the variables related to the microphysical processes can be found in relevant literature (e.g., Rutledge and Hobbs, 1983; Morrison et al., 2009; Lim and Hong, 2010).

The cloud water path is an important physical quantity in analysis of a heavy precipitation process. The liquid water path (LWP), ice water path (IWP), and total water path (TWP) are defined in Eqs. (10)–(12):

$$\text{LWP} = \int_{z_b}^{z_t} \rho_{\text{air}} q_l dz, \quad (10)$$

$$\text{IWP} = \int_{z_b}^{z_t} \rho_{\text{air}} q_i dz, \quad (11)$$

$$\text{TWP} = \int_{z_b}^{z_t} \rho_{\text{air}} q_l dz + \int_{z_b}^{z_t} \rho_{\text{air}} q_i dz, \quad (12)$$

where z_b and z_t are the model ground and top heights, respectively; ρ_{air} is air density (kg m^{-3}); and q_l and q_i represent the mixing ratio (kg kg^{-1}) of liquid- and ice-phase particles, respectively.

3. Overview of the studied case

Previous studies have well documented the characteristics of the synoptic pattern and the atmospheric stratification of the studied extreme precipitation case (e.g., Ran et al., 2021; Rao et al., 2022; Yin et al., 2022; Zhang et al., 2023). Therefore, we do not repeat those descriptions in detail here. The synoptic pattern for the studied case exhibited a quasi-stationary pattern with “two troughs and one ridge” at 500 hPa, and most areas of North China were ahead of a trough and behind the ridge, and largely under the influence of the western Pacific subtropical high. Additionally, there was strong divergence at 500 hPa over Henan Province, and especially over Zhengzhou. Therefore, extremely unstable conditions of atmospheric stratification were created with convective available potential energy ($\text{CAPE} > 2000 \text{ J kg}^{-1}$).

The stable western Pacific subtropical high, with abnormal northwestward displacement, prevented northward movement of Typhoon In-Fa, and thus Typhoon In-Fa provided strong easterly water vapor flux toward the Zhengzhou region in the lower troposphere. Meanwhile,

Typhoon Cempaka also promoted strong water vapor flux toward Zhengzhou. The overall strong southeasterly water vapor flux produced by both typhoons was blocked by the Taihang Mountains, whereupon it converged and ascended the windward slopes near Zhengzhou and contributed to the extreme precipitation event. The water vapor flux over Zhengzhou was $> 15 \text{ g s}^{-1} \text{ hPa}^{-1} \text{ cm}^{-1}$ at 850 hPa, which was approximately 1.8 times greater than that of the heavy precipitation event that occurred on 21 July 2012 in Beijing (Mao et al., 2018).

Under the condition of extreme abundance of water vapor, precipitation was mainly supported by a meso-scale convective system and an embedded mesoscale convective vortex that provided continuous upward motion, together with accumulation of water vapor and hydrometeors for the precipitation system (Fu et al., 2022).

To understand the development of the precipitation system, Fig. 2 illustrates the evolution of the observed composite reflectivity. At the initial stage of the heavy precipitation process (0300 UTC 20 July), several scattered echoes with high reflectivity appeared over Zhengzhou (Fig. 2a). Three hours later (0600 UTC), these echoes gradually converged and merged into two strong convection centers: C1 and C2 (Fig. 2d). One hour later (0700 UTC), C1 and C2 merged and formed a well-organized convective system C (Fig. 2e), with reflectivity values $> 55 \text{ dBZ}$ over the center of Zhengzhou. This convection system developed rapidly to become most vigorous two hours later (0900 UTC, Fig. 2g), with regional maximum rainfall intensity of 201.9 mm h^{-1} . Subsequently, the convective system gradually dissipated, as evidenced by the weakened echoes (Fig. 2h). Previous studies showed that the merging of convective centers can strengthen the development of cloud systems and lead to short-term heavy precipitation (Fu and Guo, 2007, 2012; Sinkevich and Krauss, 2014). The echo intensity of heavy precipitation in a convective system is generally 45–50 dBZ (Liao et al., 2010; Huang et al., 2019b), and this type of system often results in local rainstorms or even heavy rainstorms. Therefore, the continuous development and merging of the stable convective system over Zhengzhou might have directly caused this extreme rainstorm (Yin et al., 2022).

To further analyze characteristics of the vertical structure of the convective system, the vertical profile of radar echoes along the strong echo core was obtained. As multiple small convection centers merged, the size of the radar echo increased and the range of its strong center expanded (Fig. 3). The vertical structure of the radar echoes exhibited two notable features. First, after the

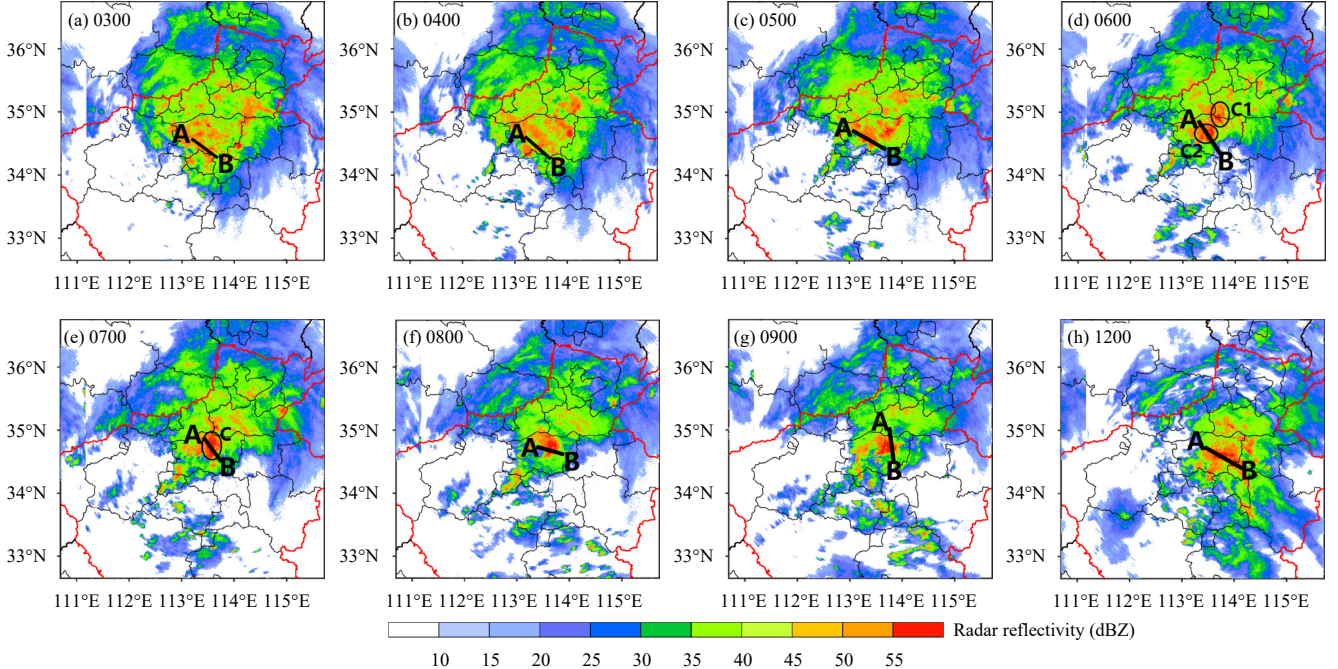


Fig. 2. Observed composite radar reflectivity (dBZ) at (a) 0300, (b) 0400, (c) 0500, (d) 0600, (e) 0700, (f) 0800, (g) 0900, and (h) 1200 UTC 20 July 2021. Black segments A–B indicate the locations of the cross-sections shown in Fig. 3. Red lines represent part of the border of Henan Province, and black lines represent the borders of cities.

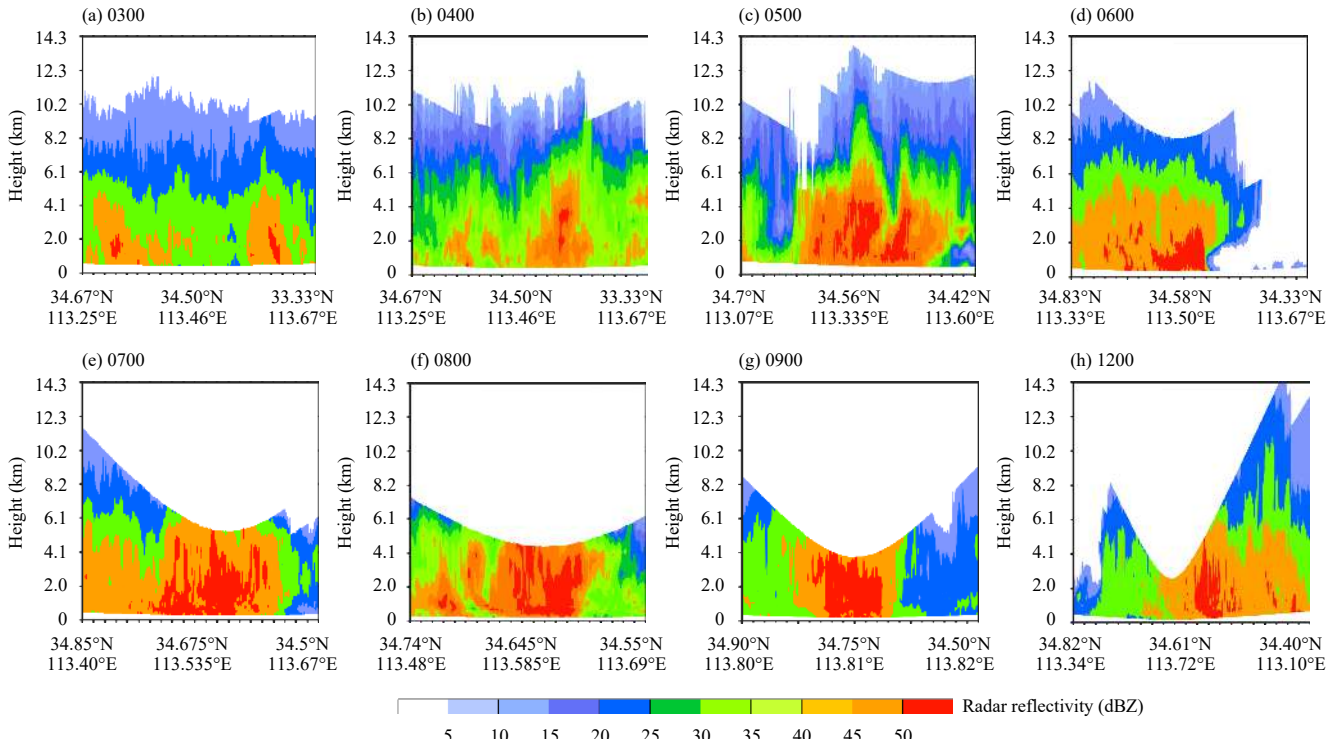


Fig. 3. Observed cross-sections of radar reflectivity (dBZ) along the strong echo core (black segment A–B in Fig. 2) at (a) 0300, (b) 0400, (c) 0500, (d) 0600, (e) 0700, (f) 0800, (g) 0900, and (h) 1200 UTC 20 July 2021.

merging of small convection centers at approximately 0700 UTC, a well-organized low-echo-centroid convective system was formed with strong echoes extending to

the ground (Figs. 3d–h). Second, throughout the precipitation stage, strong echoes > 50 dBZ were consistently located near or below the height of 5 km, indicating the

presence of abundant highly reflective hydrometeor particles below the 0°C level.

The radar observation results reveal the low-level strong echo center in the studied extreme precipitation process. Next, the corresponding characteristics of the cloud microphysical structure and the contributions of related microphysical processes were explored based on the results of the high-resolution numerical simulation.

4. Characteristics of cloud microphysics and water budget

4.1 Simulated extreme precipitation event versus observations

To verify the validity of the simulated extreme precipitation event, the simulated radar reflectivity was compared with the radar observations. The scattered weak echoes in the initial stage and the well-organized convective center in the extreme precipitation stage were well simulated by the model (Figs. 4a–e). In terms of the horizontal distribution of the composite reflectivity, the model successfully reproduced the strong echo $> 55 \text{ dBZ}$, and captured the processes of merging and strengthening

of the small cells. The position of the simulated strong echo center was consistent with that observed.

The simulated vertical structures through the strong echo center show that the model performed reasonably well in capturing both the evolution of the echo and the characteristic of a low-echo-centroid, i.e., the maximum radar reflectivity was below the 0°C level and it extended to the ground (Figs. 3, 5). This feature is different from some other heavy precipitation cases that occurred in North China, which showed that the strong echo center extended above the 0°C layer (Liu et al., 2017; Chen et al., 2021), or that there was an isolated strong echo center $> 50 \text{ dBZ}$ near or above the 0°C layer (Wang et al., 2021). Such features mean that a large amount of supercooled water was accreted by ice particles and that the cold cloud processes were strongly developed; thus, the rainwater was derived mainly from the melting of large ice particles in those other cases (Guo et al., 2015, 2020). Therefore, the different characteristics of radar echoes between the studied extreme rainfall event over Zhengzhou and those other heavy rainfall processes might indicate variation in the relative contributions of cold cloud and warm cloud microphysical processes, which is further analyzed later in this study.

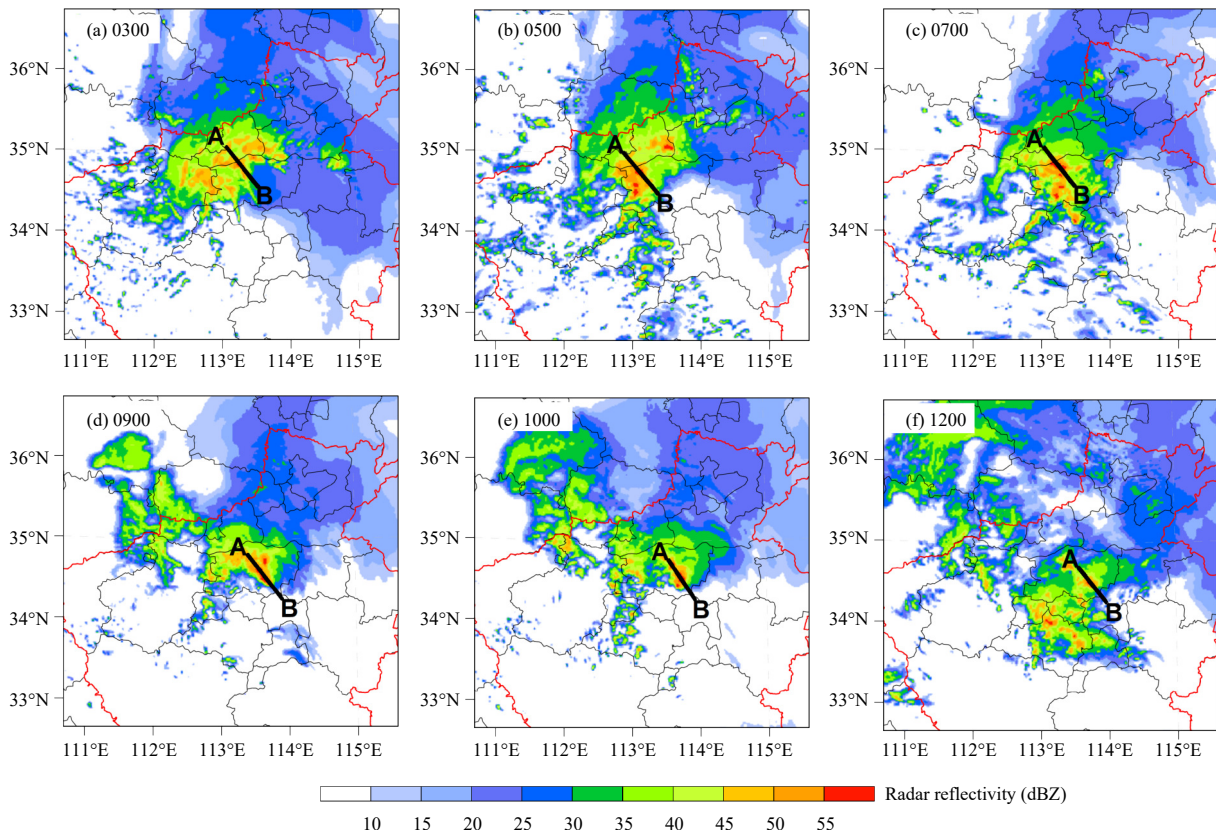


Fig. 4. Simulated composite reflectivity (dBZ) at (a) 0300, (b) 0500, (c) 0700, (d) 0900, (e) 1000, and (f) 1200 UTC 20 July 2021. Black segments A–B indicate the locations of the cross-sections shown in Fig. 5. Red lines present the border of Henan Province, and black lines represent the borders of cities.

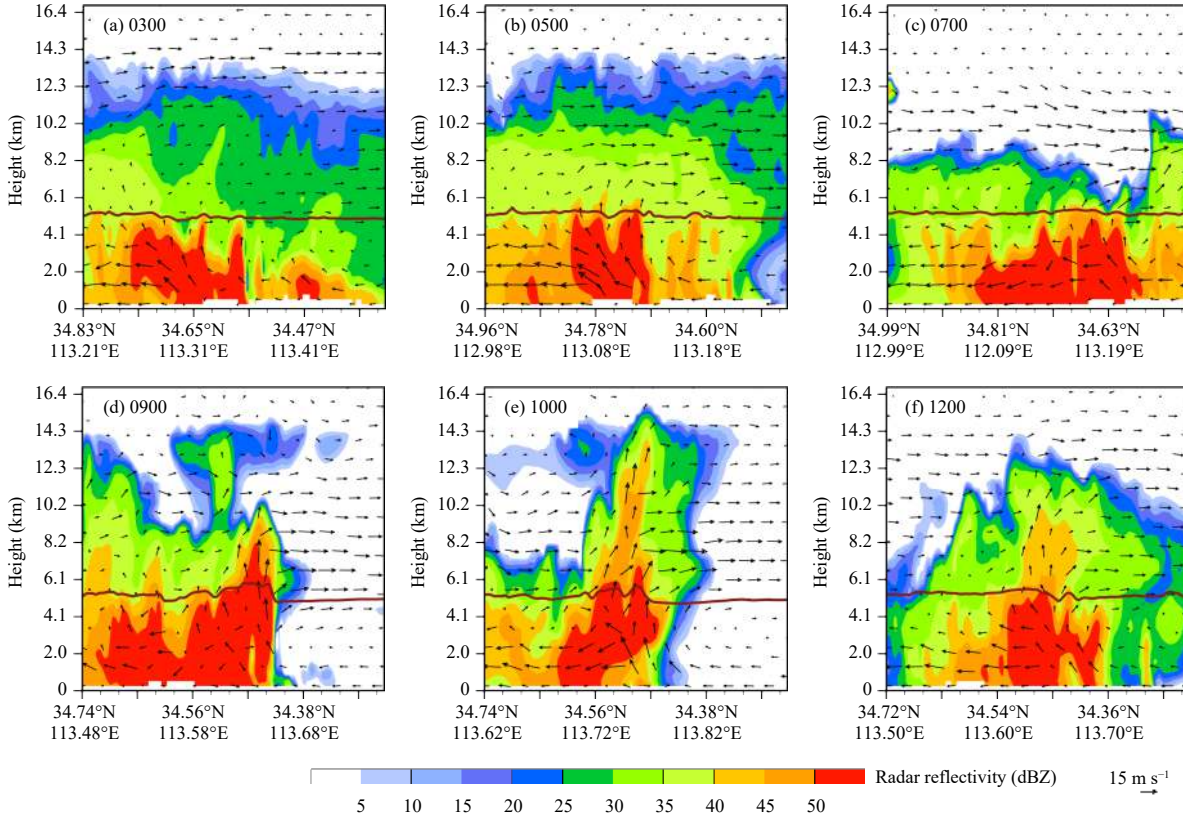


Fig. 5. Simulated cross-sections of radar reflectivity (dBZ) along the strong echo core (black segments A–B in Fig. 4) at (a) 0300, (b) 0500, (c) 0700, (d) 0900, (e) 1000, and (f) 1200 UTC 20 July 2021. Arrows indicate the wind field, and brown line represents the height of the 0°C layer.

The simulated surface precipitation and the observed surface precipitation are shown in Fig. 6 for comparison purposes. The simulation captured the general pattern of the accumulated precipitation belt across Henan Province (Figs. 6a, b). The current analysis of the simulation results focuses on the cloud microphysical processes of the extreme precipitation event in Zhengzhou; therefore, Figs. 6c and 6d compare the spatial distributions of the observed and simulated 24-h accumulated precipitation in d04, which used the horizontal resolution of 333.333 m and the LES approach. The simulated 24-h cumulative precipitation in Zhengzhou was mostly > 150 mm, and extremely heavy precipitation > 600 mm was also simulated (Figs. 6c, d). Meanwhile, the model almost perfectly simulated the distribution of hourly precipitation in Zhengzhou when the extreme precipitation occurred, with just a slight difference in the location of the high-value center (Figs. 6e, f). The differences in precipitation distribution between the observations and the simulation are acceptable given the bias of the initial conditions and the limitations in the modeled physical processes (Li et al., 2018; Tewari et al., 2022).

To further verify the capability of the model in reproducing the extreme precipitation, Fig. 7a compares the

observed and simulated precipitation intensity (mm h^{-1}) at the station/location where the maximum hourly precipitation rate occurred. The observed peak precipitation episode was from 0800 to 0900 UTC 20 July, with precipitation intensity of 201.9 mm h^{-1} , whereas the simulated peak precipitation was 199.3 mm h^{-1} (a deviation from the observations of only 2.6 mm), and it occurred 1 h later than observed, indicating that the simulation well captured the main features of the extreme rainfall event.

Figure 7b compares the time series of observed and simulated regional average hourly precipitation, and shows that the evolution of the regional precipitation was reasonably simulated, including the two precipitation peaks. Figure 7c compares the vertical profiles of the observed and simulated regional maximum radar reflectivity, and shows that below the height of approximately 5.5 km (0°C layer), the simulation perfectly reproduced the maximum radar reflectivity. The simulated radar reflectivity was larger than that observed above the height of approximately 5.5 km, which might be attributable to the relatively low spatial resolution of radar reflectivity observed at high altitudes (Wood et al., 2003). The simulated (observed) radar reflectivity below 5.5 km was approximately 60 dBZ at 1000 (0900) UTC (Fig. 7c), con-

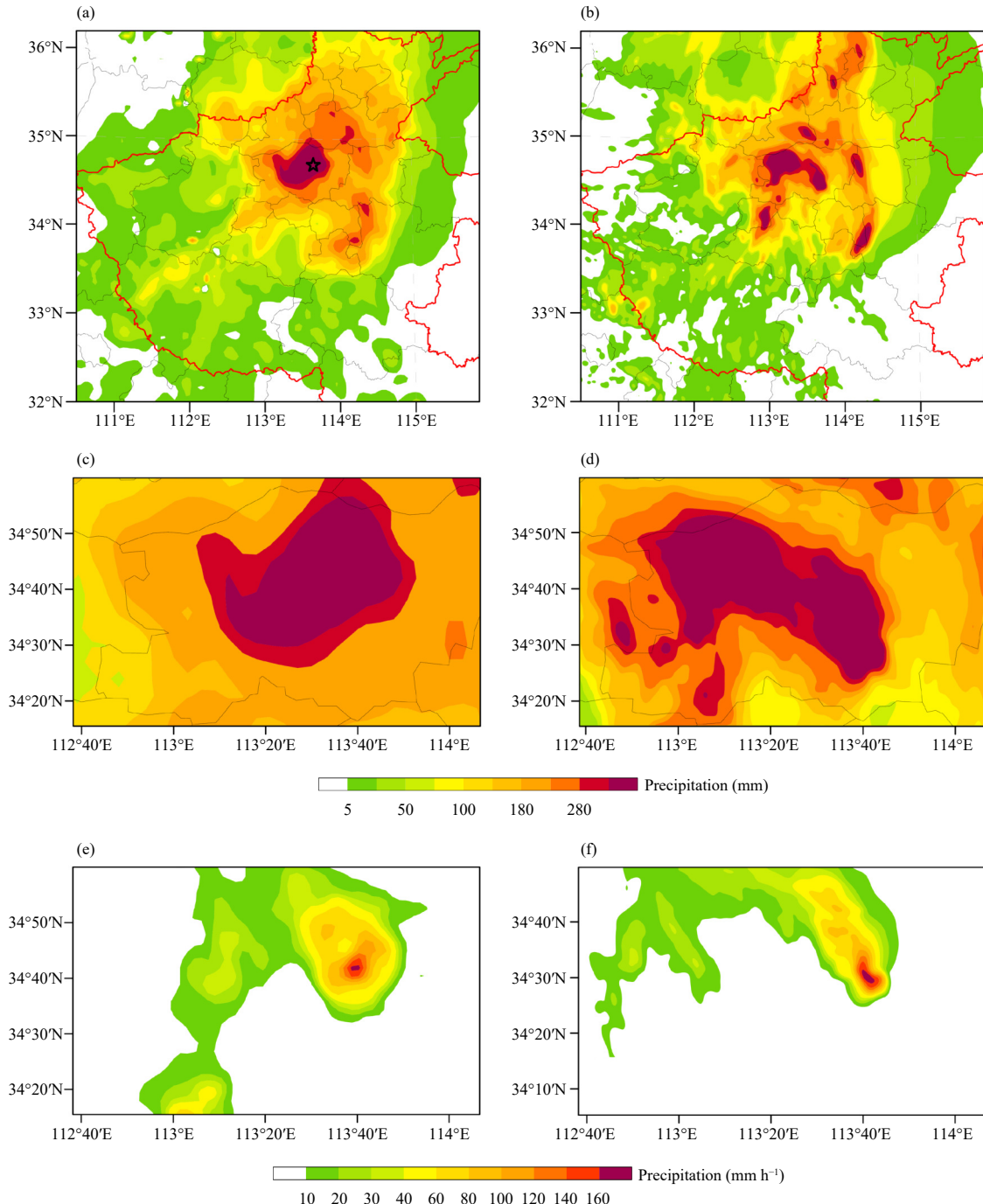


Fig. 6. (a) Observed and (b) simulated (d03) precipitation (color shading; mm) accumulated from 0000 UTC 20 to 0000 UTC 21 July 2021. Red lines represent part of the border of Henan Province, and gray lines represent the borders of cities. Bold black star represents the location of Zhengzhou station. (c, d) As in (a, b), but for d04. (e) Observed hourly precipitation during 0800–0900 UTC and (f) simulated (d04) precipitation (color shading; mm h⁻¹) during 0900–1000 UTC 20 July 2021.

sistent with the strongest precipitation. Meanwhile, both the simulations and observations indicated that the maximum radar reflectivity extended to the ground and decreased rapidly above the height of 5.5 km, as shown in the vertical sections in Figs. 3, 5.

As described above, the simulated radar reflectivity,

amount of 24-h accumulated heavy precipitation, and extreme precipitation intensity were in good agreement with those observed, demonstrating that the model simulation was close to reality and could be used to further investigate the cloud microphysical process and atmospheric water budget for this event.

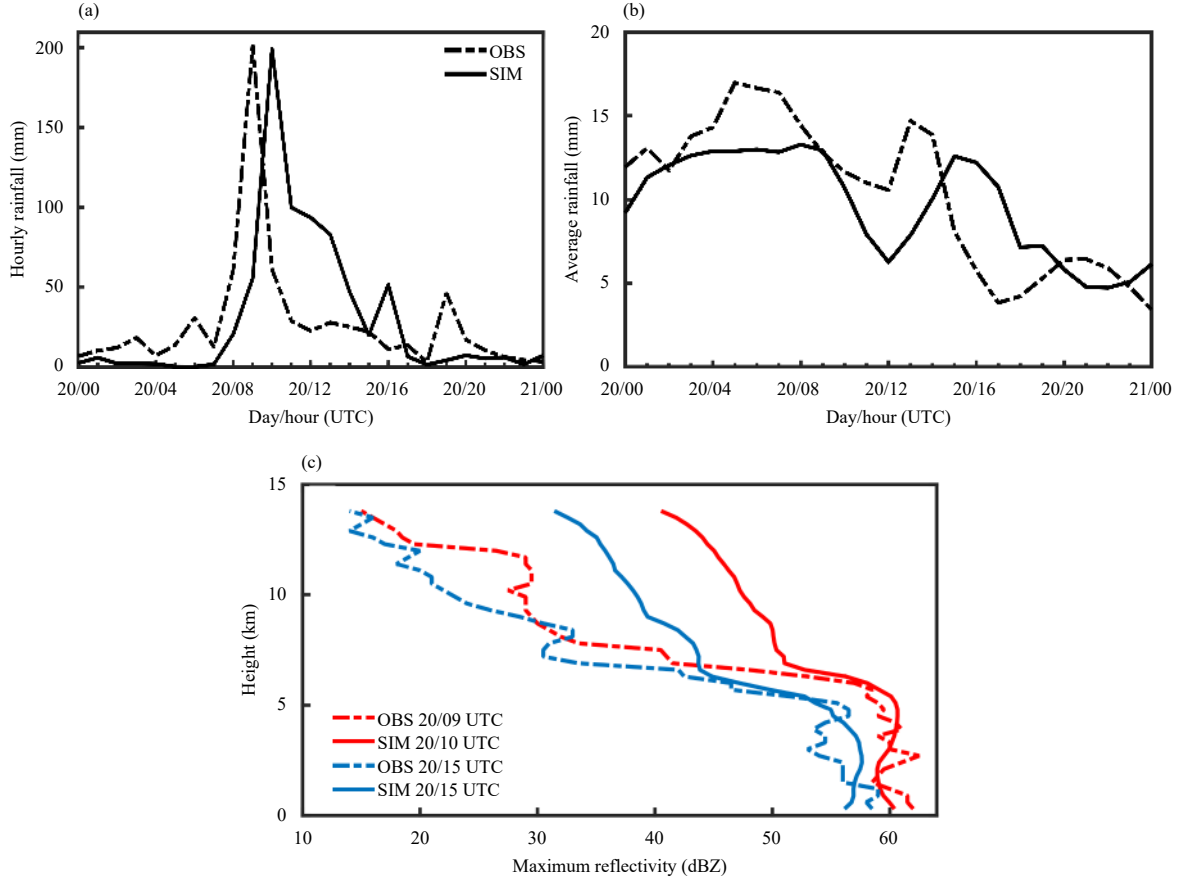


Fig. 7. (a) Time series of the observed (dashed curve) and simulated (d04) (solid curve) hourly rainfall (mm h^{-1}) at the station/location where the maximum hourly precipitation occurred near Zhengzhou (see Fig. 6 for the locations). (b) As in (a), but for the regional (d04) average hourly precipitation. (c) Vertical profiles of observed and simulated regional maximum radar reflectivity.

4.2 Contributions of atmospheric water budget processes to the extreme precipitation

Based on the calculation method described in Section 2.3, Fig. 8 shows the time series of simulated regionally

(d04) averaged rain rate (P_S), Q_{WV} , and Q_{CM} , and their ratios to P_S from 0000 UTC 20 to 0000 UTC 21 July.

The heavy precipitation process presented during 0000–1200 UTC 20 July, and the evolution of Q_{WV} followed a similar pattern to that of the precipitation rate

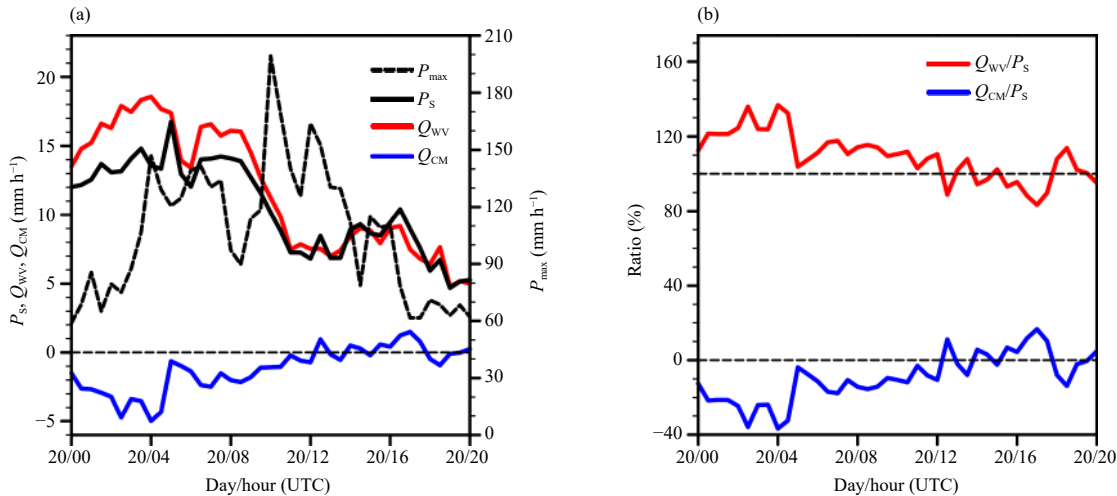


Fig. 8. (a) Time series of the regional maximum hourly rainfall rate (P_{max} , on an unfixed grid) and regional (d04) averaged P_S , Q_{WV} , and Q_{CM} . (b) Time series of the ratios of regionally averaged Q_{WV} and Q_{CM} to P_S .

(P_S ; Fig. 8a). Q_{WV} accounted for a substantial proportion of P_S , as noted in many previous studies (Gao et al., 2005; Wang Y. P. et al., 2019), indicating that the surface precipitation rate was dominated by water vapor-related processes in this case. Q_{CM} was characterized by a considerable negative contribution to P_S during almost the entire period of heavy precipitation (except at the end of precipitation), indicating that water vapor-related processes not only supplied the ground precipitation but also contributed to the development of the clouds (Fig. 8).

Figure 9 shows the evolution of the simulated regionally averaged Q_{WVL} , Q_{WVA} , and Q_{WVE} values, and their ratios to Q_{WV} . The evolution of moisture advection, Q_{WVA} , followed a pattern similar to that of Q_{WV} (Fig. 9a), and it contributed substantially to Q_{WV} (approximately 100%) during the period of heavy precipitation (Fig. 9b), indicating that the water vapor that caused the heavy precipitation was mainly advected from outside the region rather than produced through local and evaporation processes. The convergence of the large-scale water vapor flux was conducive to the development of the cloud systems and to the increase in rainfall rate. During the studied precipitation process, the values of Q_{WVL} and Q_{WVE} were small and almost negligible; however, they have been reported to reach up to 50% in some other precipitation events (Yue et al., 2009; Huang et al., 2016). Thus, Q_{WVA} was very important in this precipitation event over Zhengzhou.

Figure 10 shows the contributions of cloud-related processes to the precipitation rate. Q_{CM} includes Q_{CL} and Q_{CI} , and negative Q_{CI} values occurred during the heavy precipitation processes, while Q_{CL} values showed alternating positive and negative values (Fig. 10a). Q_{CL} , which includes Q_{CLA} and Q_{CLL} , and Q_{CI} , which includes Q_{CIL}

and Q_{CIA} , were mainly affected by Q_{CLA} and Q_{CIA} , respectively (Fig. 10b). From approximately 0000 to 1200 UTC 20 July, negative Q_{CIA} values indicated dynamic advection of hydrometeor particles to outside the region, resulting in a negative contribution to precipitation. Generally, the value of negative Q_{CIA} was greater than the value of positive Q_{CIL} , indicating that ice-phase particles were largely consumed by advection to the outside rather than through participating in the transformation of microphysical processes, which inhibited the microphysical processes of cold clouds and weakened the contribution of cold cloud processes to precipitation.

From approximately 1200 to 1600 UTC 20 July, Q_{CLA} and Q_{CIA} were positive and mainly dominated by Q_{CRAIA} and Q_{CSNOA} (Fig. 10c). This indicates that a large quantity of hydrometeors was transported to Zhengzhou during this period, contributing positively to the precipitation rate. This result supports the conclusion obtained by Sun et al. (2021) based on the optical flow field of remote sensing data, i.e., the input of hydrometeors is conducive to the maintenance of the heavy precipitation process. From approximately 0000 to 1100 UTC 20 July, Q_{CLA} was mainly negative, indicating dynamic advection of liquid water to outside the region. Moreover, ice-phase particles displayed stronger advection to the outside throughout the precipitation stage, and Q_{CIA} was dominated by the vertically integrated 3D advection of snow (Q_{CSNOA}).

Q_{CLL} consists of Q_{CCLOL} and Q_{CRAIL} , and Q_{CIL} consists of Q_{CICEL} , Q_{CSNOL} , and Q_{CGRAL} (Fig. 10d). Q_{CCLOL} , Q_{CRAIL} , Q_{CICEL} , Q_{CSNOL} , and Q_{CGRAL} alternated between negative and positive values, indicating the formation (clouds develop rapidly) and consumption of hydrometeor particles. From 0900 to 1000 UTC 20 July, Q_{CRAIL} and Q_{CSNOL} values were all positive, meaning high con-

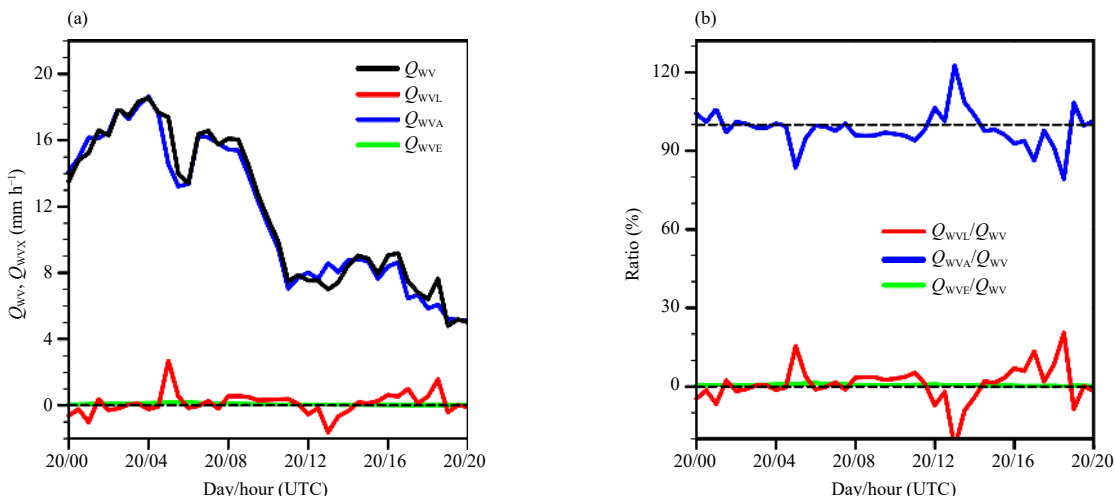


Fig. 9. (a) Time series of regionally (d04) averaged Q_{WV} , Q_{WVL} , Q_{WVA} , and Q_{WVE} . (b) Time series of the ratios of regionally averaged Q_{WVL} , Q_{WVA} , and Q_{WVE} to Q_{WV} .

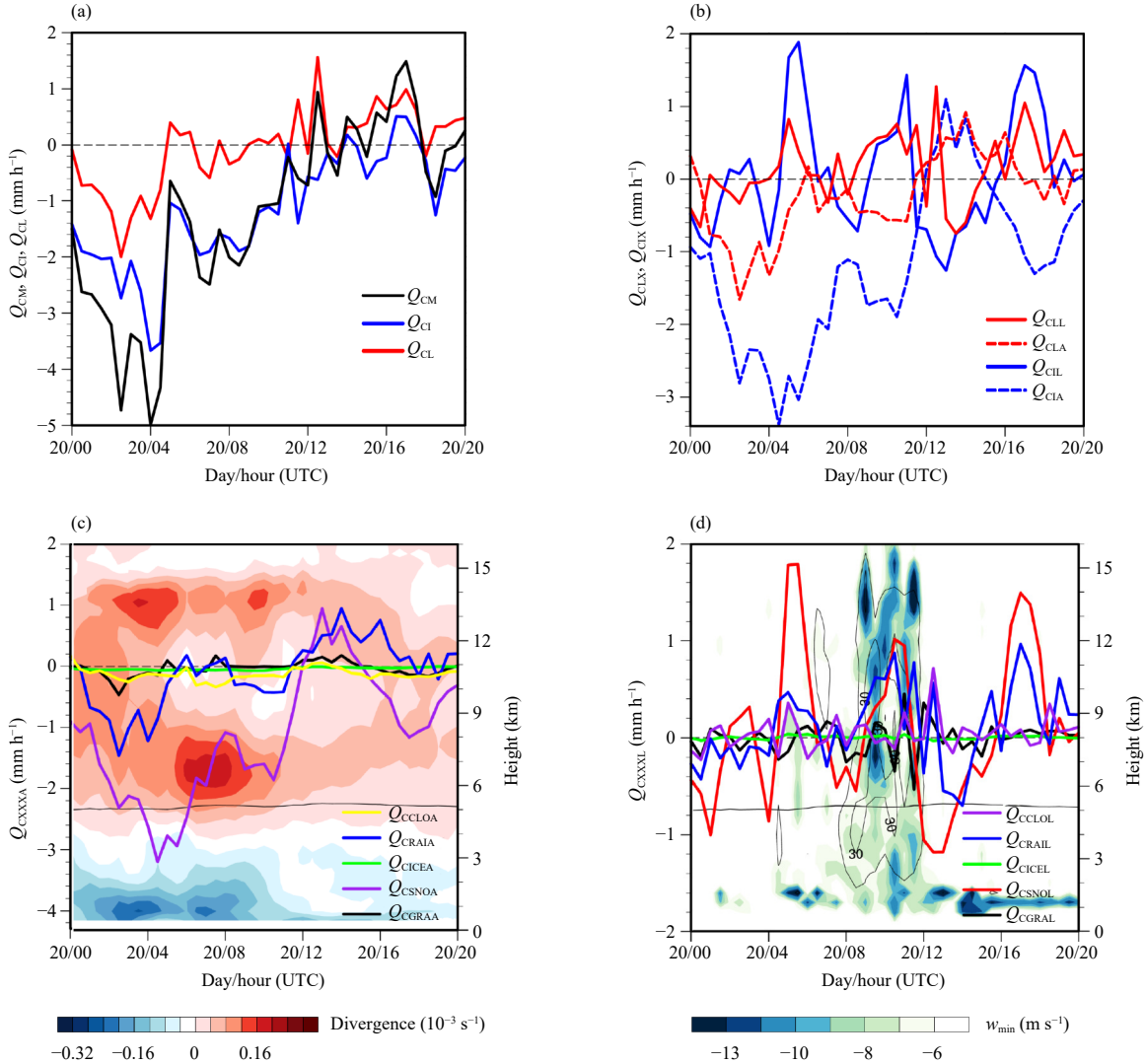


Fig. 10. (a) Time series of regionally (d04) averaged Q_{CM} , Q_{CI} , and Q_{CL} . (b) As in (a), but for Q_{CLL} , Q_{CLA} , Q_{CIL} , and Q_{CIA} . (c) Time series of regionally averaged Q_{CCLOA} , Q_{CRAIA} , Q_{CICEA} , Q_{CSNOA} , and Q_{CGRAA} and time–height contours of wind field divergence (shading; 10^{-3} s^{-1}). (d) Time series of regionally averaged Q_{CCLOL} , Q_{CRAIL} , Q_{CICEL} , Q_{CSNOL} , and Q_{CGRAL} and time–height contours of regionally maximum downdraft (w_{\min} ; shading; m s^{-1}) and updraft (black solid lines, from 22 to 38 with contour interval of 8; m s^{-1}). Gray solid line represents the height of the 0°C layer in (c, d).

sumption of hydrometeor particles and conditions favorable for extreme precipitation. At approximately 1000 UTC, the positive Q_{CSNOL} values and negative Q_{CGRAL} values reached their respective maxima, indicating an enhanced transformation process of snow to graupel, and implying that the enhancement of cold cloud processes played a positive role in the strongest hourly precipitation over Zhengzhou (0900–1000 UTC). After 0900 UTC, with enhancement of the divergence at heights above 13.5 km (Fig. 10c), the intensification of high-level convection (Fig. 10d) enhanced the cold cloud processes. Therefore, ice-phase particles were generated and converted into precipitation, and a strong downdraft appeared near the ground (Fig. 10d), which was conducive to the occurrence of the heaviest hourly precipitation at

the ground. After 1000 UTC, the positive values of Q_{CSNOL} and Q_{CRAIL} gradually decreased and shifted to negative values, indicating reduction in the consumption and increase in the formation of hydrometeor particles, leading to a weakened precipitation process at 1200 UTC and preparation for the next precipitation peak.

Q_{CIL} was dominated by the local rate of change in snow (Q_{CSNOL}), which showed a higher value in comparison with that of other ice-phase components, indicating the important and positive contribution of snow transformation to the extreme rainfall; additionally, the contribution of graupel was relatively minor.

The above analysis highlights the crucial role played by the convergence of water vapor in facilitating the precipitation process. The combination of strong conver-

gence in the lower atmosphere and strong divergence in the upper atmosphere promoted the development of the precipitation system. Moreover, the atmospheric divergence structure at and above the melting layer led to advection of ice-phase and supercooled liquid-phase particles to the outside. After 0900 UTC 20 July, weakening of the divergence near the height of 6 km and strengthening of the divergence above the height of 13.5 km weakened the advection of rainwater to outside of the region, and enhanced the high-level updraft and the downdraft near the ground, resulting in the extreme precipitation intensity of 199.3 mm h^{-1} that caused severe flooding in the urban area of Zhengzhou.

4.3 Cloud microphysical processes related to the extreme precipitation event

Figure 11a shows that the cloud water was mainly distributed between the heights of 1 and 6 km, and that the high-value center was located at the height of 5 km. The main source of cloud water was the condensation of water vapor (P_{COND}), and the main sinks were collection of cloud water by rainwater (P_{RAC}), snow (P_{SAC}), and graupel (P_{GAC}) (Fig. 11b).

Cloud ice was mainly distributed in the upper atmosphere at the height of 13 km (Fig. 12a). The main sources of cloud ice were the deposition of water vapor (P_{IDEP}) and the nucleation of primary ice (P_{IPN}), and the

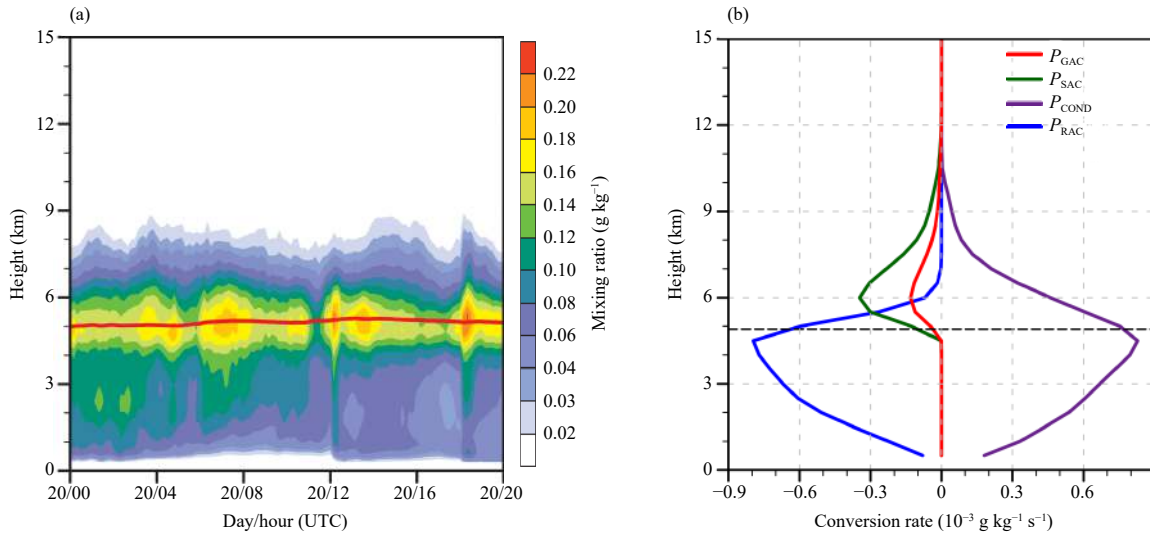


Fig. 11. (a) Time–height variations in the regionally averaged (d04) mixing ratio (shaded) of cloud water. Red solid line is the height of the 0°C layer. (b) Vertical profiles of the spatiotemporally averaged conversion rates of the main microphysical processes involving cloud water. Horizontal dashed black line represents the height of the 0°C layer.

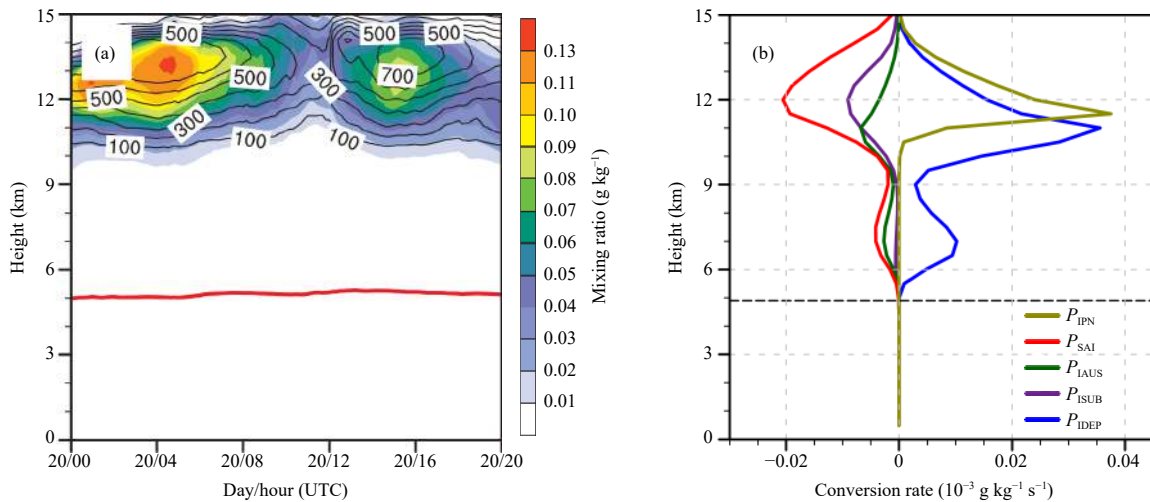


Fig. 12. (a) Time–height variations in the regionally averaged (d04) mixing ratio (shaded) and number concentrations (black contours; 10^3 kg^{-1}) of ice. Red solid line is the height of the 0°C layer. (b) Vertical profiles of the spatiotemporally averaged conversion rates of the main microphysical processes involving cloud ice. Horizontal dashed black line represents the height of the 0°C layer. P_{IAUS} represents the production rate for autoconversion of cloud ice to snow.

main sinks were the accretion of cloud ice by snow (P_{SAI}) and the sublimation of cloud ice (P_{ISUB}) (Fig. 12b).

Figure 13a shows that snow was mainly distributed at the height of 6.5 km, and that it had obvious spatial dislocation between the high-value centers of the mixing ratio and the number concentration. The high-value centers of the snow number concentration appeared at higher levels than those of the mixing ratio, suggesting that snow was mainly produced at higher altitudes and that it then fell to a low level during the growth process. The main sources of snow were the deposition of water vapor (P_{SDEP}), accretion of cloud water by snow (P_{SAC}), and accretion of rainwater by snow (P_{SAR}) (Fig. 13b). Before 0500 UTC and after 1200 UTC 20 July, the deposition of water vapor was the most important source of snow, accounting for approximately 40%–55% (Fig. 13c). Accretion of cloud water and rainwater by snow accounted for 35% and 11% of snow sources, respectively. The deposition of water vapor, as the most important source of snow, has not been regularly cited in previous studies on heavy

precipitation (Guo et al., 2015; Huang et al., 2020). This difference indicates that the water vapor supply in Zhengzhou was extremely abundant, and that the saturated air extended to the upper layer (not shown), which supported the deposition of water vapor. However, during 0500–1200 UTC 20 July, the contribution of P_{SAC} to snow formation increased and even exceeded that of P_{SDEP} (Fig. 13c), indicating enhanced cold cloud processes in the extreme precipitation stage.

Graupel particles were mainly distributed at the height of 5.5 km (Fig. 14a). The main sources of graupel were accretion of snow by rainwater and conversion to graupel (P_{RASG}) and accretion of cloud water by graupel (P_{GAC}) (Figs. 14b, c). These results differed from those of some other studies on other heavy precipitation events (Guo et al., 2020; Mao et al., 2022), and they suggested that graupel was mainly produced by accretion of rainwater by graupel. After approximately 0700 UTC 20 July, the accretion of snow by rainwater and transformation into graupel, as the main source of graupel, gradually increased with the development of the precipitation pro-

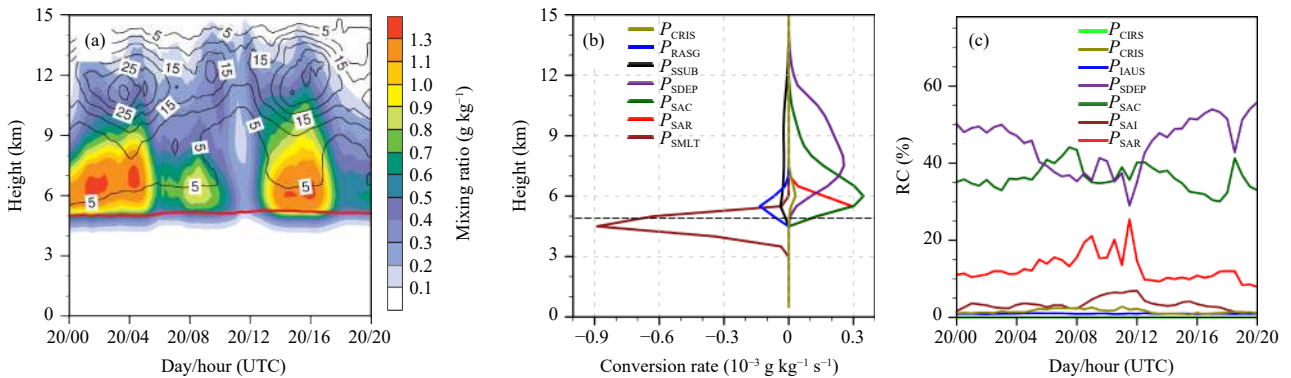


Fig. 13. (a, b) As in Figs. 12a, b, but for snow. (c) Temporal variations in the relative contributions (RCs) of microphysical processes involving snow. P_{CRIS} , P_{SSUB} , and P_{CIRS} represent the production rate for change in rainwater due to ice-rain accretion to form snow, sublimation of snow, and change in ice due to ice-rain accretion to form snow, respectively.

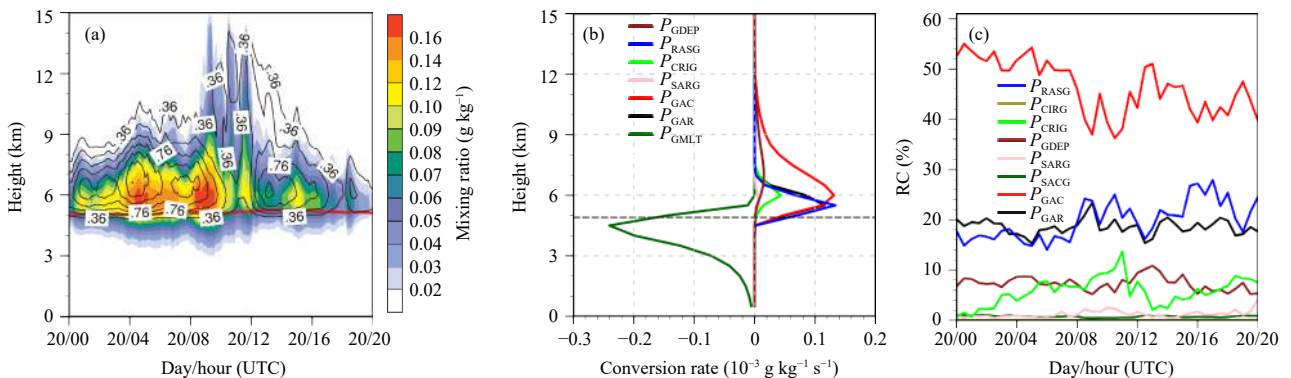


Fig. 14. As in Fig. 13, but for graupel. P_{GDEP} , P_{CRIG} , P_{SARG} , P_{GAR} , P_{GMLT} , P_{CIRG} , and P_{SACG} represent the production rate for deposition of graupel, change in rainwater due to ice-rain accretion to form graupel, accretion of rainwater by snow and conversion to graupel, accretion of rainwater by graupel, melting of graupel to rainwater, change in ice due to ice-rain accretion to form graupel, and accretion of cloud water by snow to form graupel, respectively.

cess (Fig. 14c).

Figure 15 presents the microphysical characteristics and the relative contributions of related microphysical processes involving rainwater. The rainwater was mainly below the 0°C level, with high-value centers at the height of 2.5 km (Fig. 15a). The main sinks of rainwater included accretion of rainwater by snow (P_{SAR}) above the 0°C level and evaporation of rainwater (P_{REVP}) below the 0°C level (Figs. 15b, c). The collection of cloud water by rainwater (P_{RAC}) and the melting of snow (P_{SMLT}) were the main sources (Figs. 15b, c). Cloud water collected by rainwater accounted for approximately 70% of rainwater formation, and the proportion increased slowly with the development of precipitation before 0700 UTC (Fig. 15c). The melting of snow, a second source of rainwater, accounted for only approximately 20%, while the melting of graupel accounted for approximately 5%–10% before 0500 UTC 20 July. From approximately 0500 to 1200 UTC, the contribution of graupel melting to rainwater formation increased to approximately 15% and exceeded that of snow melting (approximately 10%), reflecting enhanced cold cloud microphysical processes (Fig. 15c). When the strongest precipitation occurred at 1000 UTC, the simulated radar echo of 40 dBZ also extended to a height of approximately 12 km (Fig. 5e), which reflects enhancement of ice-phase and mixed-phase processes. These results suggest that warm cloud processes were dominant in the heavy precipitation event, and that cold cloud microphysical processes had certain positive effect on the extreme precipitation. Notably, this microphysical characteristic of the studied heavy precipitation event is different from that identified in some previous heavy precipitation events, which were mainly influenced by the melting of graupel (Gao et al., 2018; Bao et al., 2019; Li et al., 2020; Chen et al., 2021; Shu et al., 2022).

The strong water vapor convergence in the lower layer (Fig. 10c) caused a strong updraft and the warm cloud

processes developed vigorously (high rate of collection of cloud water by rainwater) (Fig. 10d). However, owing to the strong divergence during the entire precipitation process above the 0°C level, large amounts of supercooled water, cloud ice, and snow were advected to outside of the region, weakening the collection of cloud water and rainwater by snow and graupel, and preventing the formation of graupel. Therefore, the extreme rainfall process was mainly associated with warm cloud processes rather than with cold cloud processes as reported in previous studies.

4.4 Latent heating and cloud water path

Figure 16 shows the evolution of the latent heating rate due to the various cloud microphysical processes. During 0000–0900 UTC 20 July, strong convergence in the lower atmosphere (Fig. 16d) caused the formation of many cloud droplets (Fig. 11a), releasing condensational latent heat (Fig. 16a). During this period, the precipitation was dominated by relatively shallow convection, accompanied by latent heat release due to weak freezing above the 0°C level (Fig. 16b). With the development of convection, after 0500 UTC, the condensational latent heating rate below the 0°C level and the freezing and depositional latent heating rates above the 0°C level increased (Figs. 16a, b), promoting the development of updrafts (Yin et al., 2018; Guo et al., 2019). Additionally, the interaction of the large-scale circulation (strong divergence above the 0°C level and persistent strong convergence at the low levels) also promoted convection (Fig. 16d). Meanwhile, after 0600 UTC 20 July, with the production of large numbers of precipitation particles, the cooling effect from the melting of ice particles and the evaporation of rainwater below the 0°C level (Fig. 16c) favored increase in the instability of the lower atmosphere (Naeger et al., 2017). This also promoted the development of convection and enhanced the freezing process (Fig. 16b) and graupel content (Fig. 14a). When the

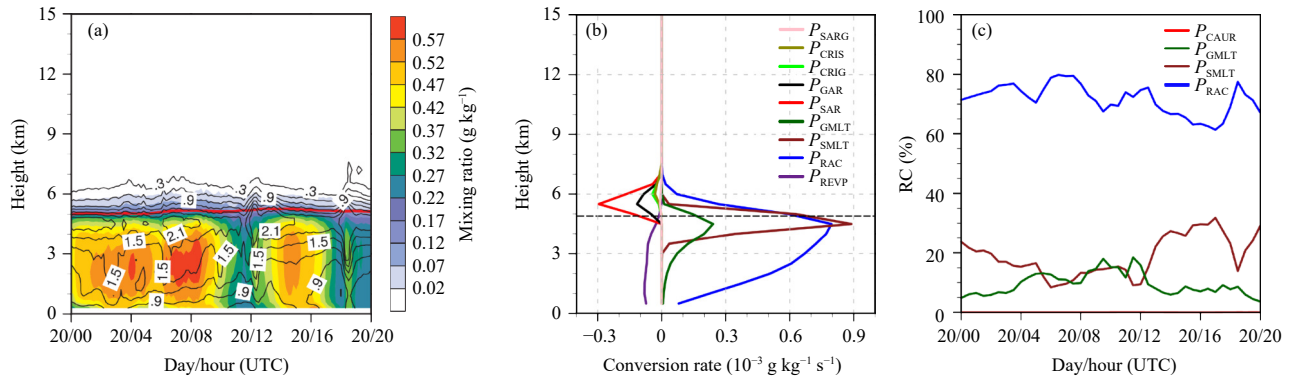


Fig. 15. As in Fig. 13, but for rainwater. P_{CAUR} represents the production rate for autoconversion of cloud water to rainwater.

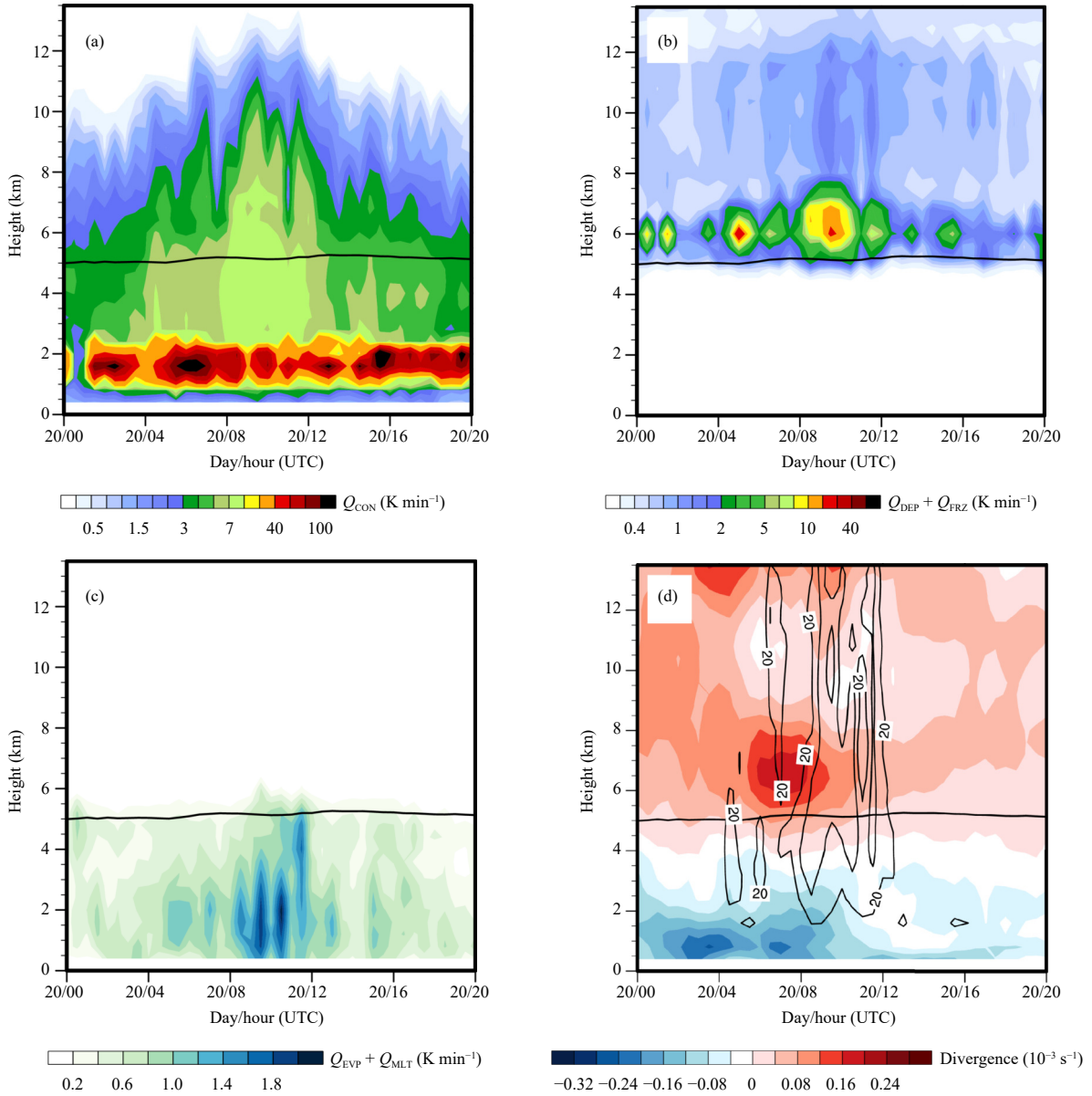


Fig. 16. Time–height variations in the regionally maximum (d04) microphysical latent heating rates of (a) condensation (Q_{CON}), (b) deposition and freezing ($Q_{DEP} + Q_{FRZ}$), and (c) evaporation and melting ($Q_{EVP} + Q_{MLT}$). (d) Time–height variations in the regionally averaged wind field divergence (shading; 10^{-3} s^{-1}) and regionally maximum updraft (black solid lines, from 20 to 34 with contour interval of 7; m s^{-1}). Solid black line is the height of the 0°C layer.

strongest precipitation occurred during 0900–1000 UTC, the rate of latent heat release reached a maximum and extended to the upper layer with enhancement of the cold cloud processes, and the strong updraft extended to the height of 12 km, illustrating that as the precipitation process developed, enhanced latent heat release might have further promoted updrafts in the middle and higher levels, and increased the height of the strong center of divergence (Fig. 16d).

Therefore, the strong divergence above the 0°C level was influenced by the interactions between the thermal processes due to the cloud microphysical processes and

the large-scale dynamic processes, leading to positive feedback to the development of the precipitation process. In addition to being controlled by the weather system, the height and intensity of the strong upper-tropospheric divergence might also have been affected by upward development of updrafts caused by the release of latent heat above the 0°C level.

Figure 17 shows the evolution of the regionally averaged and maximum LWP, IWP, and TWP. The LWP, IWP, and TWP exhibited similar changes over time. Although the average LWP was almost equal to the average IWP, the maximum LWP was obviously higher than

that of the maximum IWP, suggesting that the warm microphysical process had a more important role in the heavy precipitation event. Meanwhile, the peak of the maximum IWP and LWP appeared at 0930 UTC, corresponding to the strongest hourly precipitation during 0900–1000 UTC. The ratio of the average LWP to TWP was higher than that reported in many previous studies of heavy precipitation events (Morrison et al., 2003; Fan et al., 2008; Fowler et al., 2020; Chen et al., 2021; Shi et al., 2021).

In conclusion, the following three characteristics of this precipitation process can be obtained through analysis of the related weather processes, atmospheric water budgets, microphysical processes, latent heat release, and cloud water paths. First, the water vapor supply during this heavy precipitation was highly sufficient, which contributed to the rapid generation and transformation of hydrometeor particles, favoring continuous heavy precipitation. Second, this precipitation event was mainly dominated by warm cloud processes. The amounts of cloud water and rainwater collected by snow and graupel were comparatively less than those reported in some other heavy precipitation processes owing to the strong divergence above the 0°C level. The generation of rainwater was mainly from the collection of cloud water by rainwater rather than from the melting of graupel particles. Third, the enhancement of cold cloud processes promoted by latent heat release also played an important role in generating the most intense hourly precipitation.

5. Conclusions and discussion

In this study, the cloud microphysical processes and atmospheric water budget of an extreme precipitation event on 20 July 2021 in Zhengzhou of Henan Province,

China were investigated based on observational and ERA5 data, and analysis of the results of a WRF model nested high-resolution LES with data assimilation. The main conclusions derived are summarized as follows.

(1) The extreme precipitation event occurred under favorable atmospheric circulation, stratification, and terrain conditions. Abnormal northwestward displacement of the stable western Pacific subtropical high caused a substantial blocking effect to the northward movement of Typhoon In-Fa. Strong persistent southeasterly water vapor flux toward Zhengzhou was formed between the subtropical high and slow-moving Typhoon In-Fa, which was joined in by southerly vapor flux formed by Typhoon Cempaka, creating strong persistent water vapor flux for the extreme warm-sector precipitation event. Strong upper-level divergence over Zhengzhou under a quasi-stationary circulation pattern with “two troughs and one ridge” contributed to instability in the atmospheric stratification and caused ascending motion.

(2) The atmospheric water budget analysis indicated that water vapor-related processes accounted for a substantial proportion of the precipitation rate and that the abundance of water vapor was favorable for the rapid formation and transformation of hydrometeor particles, leading to the warm-sector heavy precipitation event. The water vapor that caused the heavy precipitation in Zhengzhou was mainly advected from outside of the region rather than being generated through local and evaporation processes.

(3) The advection of rainwater from outside Zhengzhou during the extreme precipitation event positively contributed to the precipitation rate and facilitated the maintenance of the extreme precipitation process.

(4) The precipitation contribution from the collision-coalescence process of cloud water to rainwater accounted for approximately 70% of the total, while that from

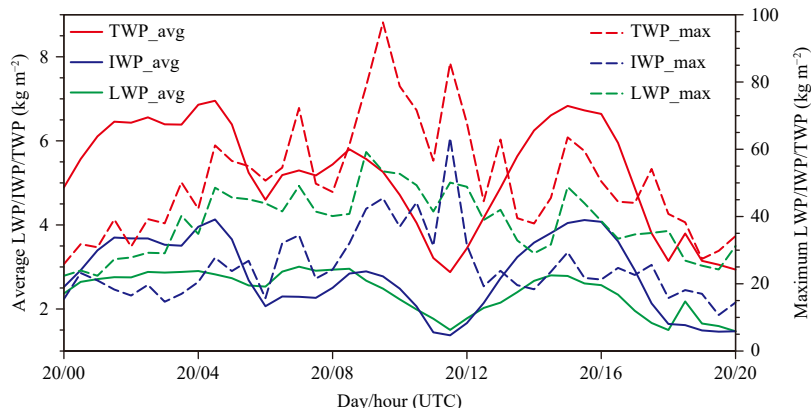


Fig. 17. Time series of the simulated regionally (d04) averaged and maximum liquid water path (LWP), ice water path (IWP), and total water path (TWP).

the melting of snow and graupel accounted for approximately only 30%. Therefore, warm cloud processes played the dominant role in the extreme precipitation event. However, enhanced cold cloud processes through latent heat release also made an important contribution during the period of most intense hourly precipitation.

In comparison with previous studies on other heavy precipitation events, this study found that warm cloud processes played a dominant role in this extreme precipitation event rather than cold microphysical processes. The results suggest that future studies of heavy precipitation events should pay more attention to warm cloud processes when a highly sufficient supply of water vapor is present.

It should also be noted that the conclusions derived in this study were based on a single warm-sector extreme precipitation case and that most of the specific results were derived from the model simulations. The simulated microphysical properties were strongly dependent on the microphysical scheme, and the microphysical scheme used for the extreme convective precipitation event has not been well validated owing to the lack of relevant observations. Therefore, the main results derived in this study pertaining to the microphysical aspects still have large uncertainties. The application of more sophisticated radar and other observations would be helpful in improving the understanding of microphysical processes in extreme precipitation events.

Acknowledgments. The authors are thankful to the Editor and all anonymous reviewers for their help in improving this manuscript.

REFERENCES

- Bao, J.-W., S. A. Michelson, and E. D. Grell, 2019: Microphysical process comparison of three microphysics parameterization schemes in the WRF model for an idealized squall-line case study. *Mon. Wea. Rev.*, **147**, 3093–3120, doi: [10.1175/MWR-D-18-0249.1](https://doi.org/10.1175/MWR-D-18-0249.1).
- Chang, W.-Y., W.-C. Lee, and Y.-C. Liou, 2015: The kinematic and microphysical characteristics and associated precipitation efficiency of subtropical convection during SoWMEX/TiM-REX. *Mon. Wea. Rev.*, **143**, 317–340, doi: [10.1175/MWR-D-14-00081.1](https://doi.org/10.1175/MWR-D-14-00081.1).
- Chen, B. J., H. Y. Wu, and M. J. Zeng, 2005: Modeling study of cloud and precipitation physical processes of the 5 July 2003 heavy rainfall in Nanjing. *Scientia Meteor. Sinica*, **25**, 26–31, doi: [10.3969/j.issn.1009-0827.2005.01.004](https://doi.org/10.3969/j.issn.1009-0827.2005.01.004). (in Chinese)
- Chen, F., and J. Dudhia, 2001: Coupling an advanced land surface-hydrology model with the Penn State-NCAR MM5 modeling system. Part I: Model implementation and sensitivity. *Mon. Wea. Rev.*, **129**, 569–585, doi: [10.1175/1520-0493\(2001\)129<0569:CAALSH>2.0.CO;2](https://doi.org/10.1175/1520-0493(2001)129<0569:CAALSH>2.0.CO;2).
- Chen, Y. H., F. Ping, S. W. Zhou, et al., 2021: Influence of microphysical processes on the initiation of the mesoscale convective system of a rainstorm over Beijing. *Atmos. Res.*, **254**, 105518, doi: [10.1016/j.atmosres.2021.105518](https://doi.org/10.1016/j.atmosres.2021.105518).
- Chyi, D., L. F. He, X. M. Wang, et al., 2022: Fine observation characteristics and thermodynamic mechanisms of extreme heavy rainfall in Henan on 20 July 2021. *J. Appl. Meteor. Sci.*, **33**, 1–15, doi: [10.11898/1001-7313.20220101](https://doi.org/10.11898/1001-7313.20220101). (in Chinese)
- De Meij, A., and J. F. Vinuesa, 2014: Impact of SRTM and Corine Land Cover data on meteorological parameters using WRF. *Atmos. Res.*, **143**, 351–370, doi: [10.1016/j.atmosres.2014.03.004](https://doi.org/10.1016/j.atmosres.2014.03.004).
- Ding, Y. H., 2015: On the study of the unprecedented heavy rainfall in Henan Province during 4–8 August 1975: Review and assessment. *Acta Meteor. Sinica*, **73**, 411–424, doi: [10.11676/qxb2015.067](https://doi.org/10.11676/qxb2015.067). (in Chinese)
- Eiserloh, A. J., Jr., and S. Chiao, 2015: Modeling studies of land-falling atmospheric rivers and orographic precipitation over northern California. *Meteor. Atmos. Phys.*, **127**, 1–16, doi: [10.1007/s00703-014-0350-4](https://doi.org/10.1007/s00703-014-0350-4).
- Fan, J. W., R. Y. Zhang, W.-K. Tao, et al., 2008: Effects of aerosol optical properties on deep convective clouds and radiative forcing. *J. Geophys. Res. Atmos.*, **113**, D08209, doi: [10.1029/2007JD009257](https://doi.org/10.1029/2007JD009257).
- Fowler, L. D., M. C. Barth, and K. Alapaty, 2020: Impact of scale-aware deep convection on the cloud liquid and ice water paths and precipitation using the Model for Prediction Across Scales (MPAS-v5.2). *Geosci. Model Dev.*, **13**, 2851–2877, doi: [10.5194/gmd-13-2851-2020](https://doi.org/10.5194/gmd-13-2851-2020).
- Franklin, C. N., G. J. Holland, and P. T. May, 2005: Sensitivity of tropical cyclone rainbands to ice-phase microphysics. *Mon. Wea. Rev.*, **133**, 2473–2493, doi: [10.1175/MWR2989.1](https://doi.org/10.1175/MWR2989.1).
- Fu, D. H., and X. L. Guo, 2007: The role of cumulus merger in a severe mesoscale convective system. *Chinese J. Atmos. Sci.*, **31**, 635–644, doi: [10.3878/j.issn.1006-9895.2007.04.08](https://doi.org/10.3878/j.issn.1006-9895.2007.04.08). (in Chinese)
- Fu, D. H., and X. L. Guo, 2012: A cloud-resolving simulation study on the merging processes and effects of topography and environmental winds. *J. Atmos. Sci.*, **69**, 1232–1249, doi: [10.1175/JAS-D-11-049.1](https://doi.org/10.1175/JAS-D-11-049.1).
- Fu, Q., Y. T. Zhang, T. X. Li, et al., 2018: Spatiotemporal complexity analysis of daily precipitation in a changing environment in Heilongjiang Province, China. *J. Hydrol. Eng.*, **23**, 04018045, doi: [10.1061/\(ASCE\)HE.1943-5584.0001703](https://doi.org/10.1061/(ASCE)HE.1943-5584.0001703).
- Fu, S.-M., Y.-C. Zhang, H.-J. Wang, et al., 2022: On the evolution of a long-lived mesoscale convective vortex that acted as a crucial condition for the extremely strong hourly precipitation in Zhengzhou. *J. Geophys. Res. Atmos.*, **127**, e2021JD036233, doi: [10.1029/2021JD036233](https://doi.org/10.1029/2021JD036233).
- Gao, S. T., X. P. Cui, Y. S. Zhou, et al., 2005: Surface rainfall processes as simulated in a cloud-resolving model. *J. Geophys. Res. Atmos.*, **110**, D10202, doi: [10.1029/2004JD005467](https://doi.org/10.1029/2004JD005467).
- Gao, W. H., L. P. Liu, J. Li, et al., 2018: The microphysical properties of convective precipitation over the Tibetan Plateau by a subkilometer resolution cloud-resolving simulation. *J. Geophys. Res. Atmos.*, **123**, 3212–3227, doi: [10.1002/2017JD027812](https://doi.org/10.1002/2017JD027812).
- Guo, C. W., H. Xiao, H. L. Yang, et al., 2015: Observation and modeling analyses of the macro- and microphysical character-

- istics of a heavy rain storm in Beijing. *Atmos. Res.*, **156**, 125–141, doi: [10.1016/j.atmosres.2015.01.007](https://doi.org/10.1016/j.atmosres.2015.01.007).
- Guo, C. W., H. Xiao, H. L. Yang, et al., 2019: Effects of cloud microphysical latent heat on a heavy rainstorm in Beijing. *Asia-Pac. J. Atmos. Sci.*, **55**, 477–492, doi: [10.1007/s13143-018-0095-y](https://doi.org/10.1007/s13143-018-0095-y).
- Guo, C. W., H. Xiao, W. Wen, et al., 2020: Effect of melting processes on the structure and precipitation of a heavy rainstorm in Beijing. *Atmos. Sci. Lett.*, **21**, e963, doi: [10.1002/asl.963](https://doi.org/10.1002/asl.963).
- He, J., M. Chen, J. Q. Zhong, et al., 2019: A study of three-dimensional radar reflectivity mosaic assimilation in the regional forecasting model for North China. *Acta Meteor. Sinica*, **77**, 210–232, doi: [10.11676/qxxb2019.005](https://doi.org/10.11676/qxxb2019.005). (in Chinese)
- Heath, N. K., H. E. Fuelberg, S. Tanelli, et al., 2017: WRF nested large-eddy simulations of deep convection during SEAC⁴RS. *J. Geophys. Res. Atmos.*, **122**, 3953–3974, doi: [10.1002/2016JD025465](https://doi.org/10.1002/2016JD025465).
- Hong, S.-Y., Y. Noh, and J. Dudhia, 2006: A new vertical diffusion package with an explicit treatment of entrainment processes. *Mon. Wea. Rev.*, **134**, 2318–2341, doi: [10.1175/MWR3199.1](https://doi.org/10.1175/MWR3199.1).
- Huang, Y. J., and X. P. Cui, 2015: Dominant cloud microphysical processes of a torrential rainfall event in Sichuan, China. *Adv. Atmos. Sci.*, **32**, 389–400, doi: [10.1007/s00376-014-4066-7](https://doi.org/10.1007/s00376-014-4066-7).
- Huang, Y. J., X. P. Cui, and X. F. Li, 2016: A three-dimensional WRF-based precipitation equation and its application in the analysis of roles of surface evaporation in a torrential rainfall event. *Atmos. Res.*, **169**, 54–64, doi: [10.1016/j.atmosres.2015.09.026](https://doi.org/10.1016/j.atmosres.2015.09.026).
- Huang, Y. J., Y. P. Wang, and X. P. Cui, 2019a: Differences between convective and stratiform precipitation budgets in a torrential rainfall event. *Adv. Atmos. Sci.*, **36**, 495–509, doi: [10.1007/s00376-019-8159-1](https://doi.org/10.1007/s00376-019-8159-1).
- Huang, Y. J., Y. B. Liu, Y. W. Liu, et al., 2019b: Mechanisms for a record-breaking rainfall in the coastal metropolitan city of Guangzhou, China: Observation analysis and nested very large eddy simulation with the WRF model. *J. Geophys. Res. Atmos.*, **124**, 1370–1391, doi: [10.1029/2018JD029668](https://doi.org/10.1029/2018JD029668).
- Huang, Y. J., Y. P. Wang, L. L. Xue, et al., 2020: Comparison of three microphysics parameterization schemes in the WRF model for an extreme rainfall event in the coastal metropolitan city of Guangzhou, China. *Atmos. Res.*, **240**, 104939, doi: [10.1016/j.atmosres.2020.104939](https://doi.org/10.1016/j.atmosres.2020.104939).
- Iacono, M. J., J. S. Delamere, E. J. Mlawer, et al., 2008: Radiative forcing by long-lived greenhouse gases: Calculations with the AER radiative transfer models. *J. Geophys. Res. Atmos.*, **113**, D13103, doi: [10.1029/2008JD009944](https://doi.org/10.1029/2008JD009944).
- Kain, J. S., 2004: The Kain–Fritsch convective parameterization: An update. *J. Appl. Meteor.*, **43**, 170–181, doi: [10.1175/1520-0450\(2004\)043<0170:TKCPAU>2.0.CO;2](https://doi.org/10.1175/1520-0450(2004)043<0170:TKCPAU>2.0.CO;2).
- Kang, S.-L., and G. H. Bryan, 2011: A large-eddy simulation study of moist convection initiation over heterogeneous surface fluxes. *Mon. Wea. Rev.*, **139**, 2901–2917, doi: [10.1175/MWR-D-10-05037.1](https://doi.org/10.1175/MWR-D-10-05037.1).
- Lazarus, S. M., C. M. Ciliberti, J. D. Horel, et al., 2002: Near-real-time applications of a mesoscale analysis system to complex terrain. *Wea. Forecasting*, **17**, 971–1000, doi: [10.1175/1520-0434\(2002\)017<0971:NRTAOA>2.0.CO;2](https://doi.org/10.1175/1520-0434(2002)017<0971:NRTAOA>2.0.CO;2).
- Li, C., Y. Deng, C. G. Cui, et al., 2020: Hydrometeor budget of the Meiyu frontal rainstorms associated with two different atmospheric circulation patterns. *J. Geophys. Res. Atmos.*, **125**, e2019JD031955, doi: [10.1029/2019JD031955](https://doi.org/10.1029/2019JD031955).
- Li, X., Z. X. Pu, and Z. Q. Gao, 2021: Effects of roll vortices on the evolution of Hurricane Harvey during landfall. *J. Atmos. Sci.*, **78**, 1847–1867, doi: [10.1175/JAS-D-20-0270.1](https://doi.org/10.1175/JAS-D-20-0270.1).
- Li, X. R., K. Fan, and E. T. Yu, 2018: A heavy rainfall event in autumn over Beijing—Atmospheric circulation background and hindcast simulation using WRF. *J. Meteor. Res.*, **32**, 503–515, doi: [10.1007/s13351-018-7168-9](https://doi.org/10.1007/s13351-018-7168-9).
- Liao, Y. S., J. Li, X. F. Wang, et al., 2010: A meso- β scale analysis of the torrential rain event in Jinan in 18 July 2007. *Acta Meteor. Sinica*, **68**, 944–956, doi: [10.11676/qxxb2010.089](https://doi.org/10.11676/qxxb2010.089). (in Chinese)
- Lim, K.-S. S., and S.-Y. Hong, 2010: Development of an effective double-moment cloud microphysics scheme with prognostic cloud condensation nuclei (CCN) for weather and climate models. *Mon. Wea. Rev.*, **138**, 1587–1612, doi: [10.1175/2009MWR2968.1](https://doi.org/10.1175/2009MWR2968.1).
- Liu, S. N., and X. P. Cui, 2018: Diagnostic analysis of rate and efficiency of torrential rainfall associated with Bilis (2006). *Chinese J. Atmos. Sci.*, **42**, 192–208, doi: [10.3878/j.issn.1006-9895.1704.17148](https://doi.org/10.3878/j.issn.1006-9895.1704.17148). (in Chinese)
- Liu, Y., Z. M. Liang, and Y. P. Li, 2017: Observational and simulation study of a local severe precipitation event caused by a cold vortex over Northeast China. *Adv. Meteor.*, **2017**, 2764–340, doi: [10.1155/2017/2764340](https://doi.org/10.1155/2017/2764340).
- Liu, Y. J., S. G. Miao, F. Hu, et al., 2018: Large eddy simulation of flow field over the Xiaohaituo Mountain division for the 24th Winter Olympic Games. *Plateau Meteor.*, **37**, 1388–1401. (in Chinese)
- Lu, T. T., X. P. Cui, Q. L. Zou, et al., 2021: Atmospheric water budget associated with a local heavy precipitation event near the Central Urban Area of Beijing Metropolitan Region. *Atmos. Res.*, **260**, 105600, doi: [10.1016/j.atmosres.2021.105600](https://doi.org/10.1016/j.atmosres.2021.105600).
- Mao, J. H., F. Ping, L. Yin, et al., 2018: A study of cloud microphysical processes associated with torrential rainfall event over Beijing. *J. Geophys. Res. Atmos.*, **123**, 8768–8791, doi: [10.1029/2018JD028490](https://doi.org/10.1029/2018JD028490).
- Mao, Z., Z. P. Zhu, R. Y. Zhang, et al., 2022: The impact of different cloud microphysics parameterization schemes on the simulation of a heavy rainfall event over the Tibetan Plateau. *J. Trop. Meteor.*, **38**, 81–90. (in Chinese)
- Morrison, H., M. D. Shupe, and J. A. Curry, 2003: Modeling clouds observed at SHEBA using a bulk microphysics parameterization implemented into a single-column model. *J. Geophys. Res. Atmos.*, **108**, 4255, doi: [10.1029/2002JD00229](https://doi.org/10.1029/2002JD00229).
- Morrison, H., G. Thompson, and V. Tatarki, 2009: Impact of cloud microphysics on the development of trailing stratiform precipitation in a simulated squall line: Comparison of one- and two-moment schemes. *Mon. Wea. Rev.*, **137**, 991–1007, doi: [10.1175/2008MWR2556.1](https://doi.org/10.1175/2008MWR2556.1).
- Naeger, A. R., B. A. Colle, and A. Molthan, 2017: Evaluation of cloud microphysical schemes for a warm frontal snowband during the GPM Cold Season Precipitation Experiment (GCPEX). *Mon. Wea. Rev.*, **145**, 4627–4650, doi: [10.1175/MWR-D-17-0081.1](https://doi.org/10.1175/MWR-D-17-0081.1).

- Ran, L. K., S. W. Li, Y. S. Zhou, et al., 2021: Observational analysis of the dynamic, thermal, and water vapor characteristics of the “7.20” extreme rainstorm event in Henan Province, 2021. *Chinese J. Atmos. Sci.*, **45**, 1366–1383. (in Chinese)
- Rao, J., J. Xie, Y. Cao, et al., 2022: Record flood-producing rainstorms of July 2021 and August 1975 in Henan of China: Comparative synoptic analysis using ERA5. *J. Meteor. Res.*, **36**, 809–823, doi: [10.1007/s13351-022-2066-6](https://doi.org/10.1007/s13351-022-2066-6).
- Rauber, R. M., L. S. Olthoff, M. K. Ramamurthy, et al., 2000: The relative importance of warm rain and melting processes in freezing precipitation events. *J. Appl. Meteor. Climatol.*, **39**, 1185–1195, doi: [10.1175/1520-0450\(2000\)039<1185:TRIOWR>2.0.CO;2](https://doi.org/10.1175/1520-0450(2000)039<1185:TRIOWR>2.0.CO;2).
- Rutledge, S. A., and P. V. Hobbs, 1983: The mesoscale and microscale structure and organization of clouds and precipitation in midlatitude cyclones. VIII: A model for the “seeder-feeder” process in warm-frontal rainbands. *J. Atmos. Sci.*, **40**, 1185–1206, doi: [10.1175/1520-0469\(1983\)040<1185:TMAMSA>2.0.CO;2](https://doi.org/10.1175/1520-0469(1983)040<1185:TMAMSA>2.0.CO;2).
- Saunders, R. W., 1993: Note on the Advanced Microwave Sounder Unit. *Bull. Amer. Meteor. Soc.*, **74**, 2211–2212, doi: [10.1175/1520-0477-74.11.2211](https://doi.org/10.1175/1520-0477-74.11.2211).
- Shen, X. Y., N. Zhang, and X. F. Li, 2011: Effects of large-scale forcing and ice clouds on pre-summer heavy rainfall over southern China in June 2008: A partitioning analysis based on surface rainfall budget. *Atmos. Res.*, **101**, 155–163, doi: [10.1016/j.atmosres.2011.02.001](https://doi.org/10.1016/j.atmosres.2011.02.001).
- Shi, R. L., Y. Yin, Q. Chen, et al., 2021: Numerical simulation of aerosol effects on the physical processes of hail formation in Xinjiang. *Chinese J. Atmos. Sci.*, **45**, 107–122. (in Chinese)
- Shu, W. X., H. Xiao, D. H. Fu, et al., 2022: Effects of cloud condensation nuclei concentration on the evolution of severe convective storms. *Atmos. Res.*, **276**, 106252, doi: [10.1016/j.atmosres.2022.106252](https://doi.org/10.1016/j.atmosres.2022.106252).
- Sinkevich, A. A., and T. W. Krauss, 2014: Changes in thunderstorm characteristics due to feeder cloud merging. *Atmos. Res.*, **142**, 124–132, doi: [10.1016/j.atmosres.2013.06.007](https://doi.org/10.1016/j.atmosres.2013.06.007).
- Skamarock, W. C., J. B. Klemp, J. Dudhia, et al., 2008: A Description of the Advanced Research WRF Version 3. No. NCAR/TN-475+STR, University Corporation for Atmospheric Research, Boulder, 113 pp., doi: [10.5065/D68S4MVH](https://doi.org/10.5065/D68S4MVH).
- Song, H.-J., and B.-J. Sohn, 2018: An evaluation of WRF microphysics schemes for simulating the warm-type heavy rain over the Korean Peninsula. *Asia-Pac. J. Atmos. Sci.*, **54**, 225–236, doi: [10.1007/s13143-018-0006-2](https://doi.org/10.1007/s13143-018-0006-2).
- Song, H.-J., B.-J. Sohn, S.-Y. Hong, et al., 2017: Idealized numerical experiments on the microphysical evolution of warm-type heavy rainfall. *J. Geophys. Res. Atmos.*, **122**, 1685–1699, doi: [10.1002/2016JD025637](https://doi.org/10.1002/2016JD025637).
- Stevens, B., C. Acquistapace, A. Hansen, et al., 2020: The added value of large-eddy and storm-resolving models for simulating clouds and precipitation. *J. Meteor. Soc. Japan*, **98**, 395–435, doi: [10.2151/jmsj.2020-021](https://doi.org/10.2151/jmsj.2020-021).
- Su, A. F., X. N. Lyu, L. M. Cui, et al., 2021: The basic observational analysis of “7.20” extreme rainstorm in Zhengzhou. *Torr. Rain Dis.*, **40**, 445–454, doi: [10.3969/j.issn.1004-9045.2021.05.001](https://doi.org/10.3969/j.issn.1004-9045.2021.05.001). (in Chinese)
- Sun, Y., H. Xiao, H. L. Yang, et al., 2021: Analysis of dynamic conditions and hydrometeor transport of Zhengzhou super-heavy rainfall event on 20 July 2021 based on optical flow field of remote sensing data. *Chinese J. Atmos. Sci.*, **45**, 1384–1399. (in Chinese)
- Tellman, B., J. A. Sullivan, C. Kuhn, et al., 2021: Satellite imaging reveals increased proportion of population exposed to floods. *Nature*, **596**, 80–86, doi: [10.1038/s41586-021-03695-w](https://doi.org/10.1038/s41586-021-03695-w).
- Tewari, M., F. Chen, J. Dudhia, et al., 2022: Understanding the sensitivity of WRF hindcast of Beijing extreme rainfall of 21 July 2012 to microphysics and model initial time. *Atmos. Res.*, **271**, 106085, doi: [10.1016/j.atmosres.2022.106085](https://doi.org/10.1016/j.atmosres.2022.106085).
- Van Weverberg, K., N. P. M. van Lipzig, and L. Delobbe, 2011: The impact of size distribution assumptions in a bulk one-moment microphysics scheme on simulated surface precipitation and storm dynamics during a low-topped supercell case in Belgium. *Mon. Wea. Rev.*, **139**, 1131–1147, doi: [10.1175/2010MWR3481.1](https://doi.org/10.1175/2010MWR3481.1).
- Wang, G. L., D.-L. Zhang, and J. S. Sun, 2021: A multiscale analysis of a nocturnal extreme rainfall event of 14 July 2017 in Northeast China. *Mon. Wea. Rev.*, **149**, 173–187, doi: [10.1175/MWR-D-20-0232.1](https://doi.org/10.1175/MWR-D-20-0232.1).
- Wang, M. J., K. Zhao, M. Xue, et al., 2016: Precipitation microphysics characteristics of a Typhoon Matmo (2014) rainband after landfall over eastern China based on polarimetric radar observations. *J. Geophys. Res. Atmos.*, **121**, 12,415–12,433, doi: [10.1002/2016JD025307](https://doi.org/10.1002/2016JD025307).
- Wang, X. H., X. P. Cui, and S. F. Hao, 2019: Diagnostic and numerical study on surface rainfall processes associated with tropical cyclone Souledor (2015) over the ocean. *Chinese J. Atmos. Sci.*, **43**, 417–436, doi: [10.3878/j.issn.1006-9895.1804.18118](https://doi.org/10.3878/j.issn.1006-9895.1804.18118). (in Chinese)
- Wang, Y. P., Y. J. Huang, and X. P. Cui, 2019: Surface rainfall processes during the genesis period of tropical cyclone Durian (2001). *Adv. Atmos. Sci.*, **36**, 451–464, doi: [10.1007/s00376-018-8157-8](https://doi.org/10.1007/s00376-018-8157-8).
- Wood, V. T., R. A. Brown, and S. V. Vasiloff, 2003: Improved detection using negative elevation angles for mountaintop WSR-88Ds. Part II: Simulations of the three radars covering Utah. *Wea. Forecasting*, **18**, 393–403, doi: [10.1175/1520-0434\(2003\)18<393:IDUNEA>2.0.CO;2](https://doi.org/10.1175/1520-0434(2003)18<393:IDUNEA>2.0.CO;2).
- Wu, X. S., S. L. Guo, J. B. Yin, et al., 2018: On the event-based extreme precipitation across China: Time distribution patterns, trends, and return levels. *J. Hydrol.*, **562**, 305–317, doi: [10.1016/j.jhydrol.2018.05.028](https://doi.org/10.1016/j.jhydrol.2018.05.028).
- Wu, Y.-C., M.-J. Yang, and P.-H. Lin, 2020: Evolution of water budget and precipitation efficiency of mesoscale convective systems over the South China Sea. *Terr. Atmos. Ocean. Sci.*, **31**, 141–158, doi: [10.3319/TAO.2019.07.17.01](https://doi.org/10.3319/TAO.2019.07.17.01).
- Wu, Z. N., Y. H. Cui, and Y. Guo, 2021: A case study of flood risk evaluation based on energy theory and cloud model in Anyang region, China. *Water*, **13**, 420, doi: [10.3390/w13040420](https://doi.org/10.3390/w13040420).
- Xu, H. Y., G. Q. Zhai, and X. F. Li, 2018: Convective-stratiform rainfall separation of typhoon Fitow (2013): A 3D WRF modeling study. *Terr. Atmos. Ocean. Sci.*, **29**, 315–329, doi: [10.3319/TAO.2017.10.11.01](https://doi.org/10.3319/TAO.2017.10.11.01).
- Yang, H.-L., H. Xiao, and C.-W. Guo, 2015: Structure and evolution of a squall line in northern China: A case study. *Atmos. Res.*, **158–159**, 139–157, doi: [10.1016/j.atmosres.2015.02.012](https://doi.org/10.1016/j.atmosres.2015.02.012).
- Yin, J.-F., D.-H. Wang, Z.-M. Liang, et al., 2018: Numerical study

- of the role of microphysical latent heating and surface heat fluxes in a severe precipitation event in the warm sector over Southern China. *Asia-Pac. J. Atmos. Sci.*, **54**, 77–90, doi: [10.1007/s13143-017-0061-0](https://doi.org/10.1007/s13143-017-0061-0).
- Yin, J. F., H. D. Gu, X. D. Liang, et al., 2022: A possible dynamic mechanism for rapid production of the extreme hourly rainfall in Zhengzhou City on 20 July 2021. *J. Meteor. Res.*, **36**, 6–25, doi: [10.1007/s13351-022-1166-7](https://doi.org/10.1007/s13351-022-1166-7).
- Yue, C. J., S. W. Shou, and X. F. Li, 2009: Water vapor, cloud, and surface rainfall budgets associated with the landfall of Typhoon Krosa (2007): A two-dimensional cloud-resolving modeling study. *Adv. Atmos. Sci.*, **26**, 1198–1208, doi: [10.1007/s00376-009-8135-2](https://doi.org/10.1007/s00376-009-8135-2).
- Zhang, D. L., and R. A. Anthes, 1982: A high-resolution model of the planetary boundary layer—Sensitivity tests and comparisons with SESAME-79 data. *J. Appl. Meteor.*, **21**, 1594–1609, doi: [10.1175/1520-0450\(1982\)021<1594:AHRMOT>2.0.CO;2](https://doi.org/10.1175/1520-0450(1982)021<1594:AHRMOT>2.0.CO;2).
- Zhang, G. S., J. Y. Mao, W. Hua, et al., 2023: Synergistic effect of the planetary-scale disturbance, typhoon and meso- β -scale convective vortex on the extremely intense rainstorm on 20 July 2021 in Zhengzhou. *Adv. Atmos. Sci.*, **40**, 428–446, doi: [10.1007/s00376-022-2189-9](https://doi.org/10.1007/s00376-022-2189-9).
- Zhang, Q., X. H. Gu, V. P. Singh, et al., 2017: Timing of floods in southeastern China: Seasonal properties and potential causes. *J. Hydrol.*, **552**, 732–744, doi: [10.1016/j.jhydrol.2017.07.039](https://doi.org/10.1016/j.jhydrol.2017.07.039).
- Zhang, Y., 2014: Spatial-temporal distribution characteristics of rainstorm days from 1961 to 2010 in Henan Province. *Meteor. Environ. Sci.*, **37**, 103–106, doi: [10.3969/j.issn.1673-7148.2014.01.017](https://doi.org/10.3969/j.issn.1673-7148.2014.01.017). (in Chinese)
- Zhu, T., and D.-L. Zhang, 2006: Numerical simulation of Hurricane Bonnie (1998). Part II: Sensitivity to varying cloud microphysical processes. *J. Atmos. Sci.*, **63**, 109–126, doi: [10.1175/JAS3599.1](https://doi.org/10.1175/JAS3599.1).
- Zhu, X. L., D. Li, W. Y. Zhou, et al., 2017: An idealized LES study of urban modification of moist convection. *Quart. J. Roy. Meteor. Soc.*, **143**, 3228–3243, doi: [10.1002/qj.3176](https://doi.org/10.1002/qj.3176).

Tech & Copy Editor: Qi WANG